Iraqi Geological Journal

Journal homepage: https://www.igj-iraq.org

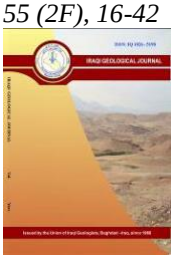

Geochemical and Characteristics of Mafic and Ultramafic Rocks of the Suprasubduction Zone Mawat Ophiolite, NE Iraq

Heider S. Al Humadi [1,2,*], Markku Väisänen [2], Sabah A. Ismail [3]

[1] Department of Applied Geology, College of Sciences, University of Babylon, Iraq

[2] Department of Geography and Geology, 20014 University of Turku, Finland

[3] Department of Applied Geology, College of Sciences, University of Kirkuk, Iraq

[*] Corresponding author (sci.heider.humadi@uobabylon.edu.iq)

Received:
3 June 2022

Accepted:
8 September 2022

Published:
31 December 2022

Abstract

New geochemical data were presented for the mafic (basalts and gabbros) and ultramafic (dunites, serpentinites and pyroxenites) rocks from the Mawat ophiolite exposed in the Zagros suture zone in northeastern Iraq. The mantle section of the ophiolite is composed of serpentinized peridotites, harzburgites, dunites, chromitites and pyroxenite dykes. The crustal section is composed of layered amphibole-rich gabbros, pegmatitic gabbros as well as basalts and minor felsic dykes. The ultramafic rocks are highly depleted in the LILEs and most of the HFSEs. The mafic rocks are tholeiitic, characterized by depletion of LREEs and display a positive trend from LREE to HREE with low Ti/V ratios. The younger gabbros are mostly calc-alkaline, characterized by enrichments of LREE with a negative REE trend and high Ti/V ratios. The basaltic and ultramafic samples plot below the N-MORB reference line suggesting that these elements have been mobile. They fall within the boninitic field in the Ti/V diagram and are related to the subduction initiation setting. The younger gabbros are related to rifting which postdated the formation of ophiolite. These geochemical data are consistent with the subduction-related suprasubduction zone tectonic setting.

Keywords: Neotethyan; Zagros; Suprasubduction; Ophiolite; Geochemistry; Mawat ophiolite

1. Introduction

Ophiolites are remnants of ancient oceanic crust and upper mantle. They are located along the destructive continental margins emplaced there by obduction because of accretional and collisional tectonics after the formation of oceanic crust. They have formed in various tectonic settings, such as mid-ocean ridges (MOR), suprasubduction zones (SSZ), intra-oceanic arcs, volcanic arc, forearcs, backarcs and rifting of continental margins (Saccani et al., 2015).

Ophiolites are reported from various parts of the world with ages ranging from Archean to Cenozoic (Furnes et al., 2014). For example, Archean suprasubduction zone ophiolites occur along the margin of microcontinent in the North China Craton (Santosh et al., 2016) and a Proterozoic 870-627 Ma old ophiolite suite in the Arabian Shield (Dilek and Ahmed, 2003).

DOI: 10.46717/igj.55.2F.2ms-2022-12-17

In the Alpine-Himalayan Orogenic Belt, the ophiolites are classified in two age groups: the Jurassic group (170 to 140 Ma old) and the Cretaceous group (125 Ma to 90 Ma old), but minor Triassic/Permian group is also reported (Furnes et al., 2020). The Cenozoic ophiolites also occur within the Alpine-Himalayan Orogenic Belt. The Eocene ophiolites, that occur along the Iran-Iraq border from Kermanshah in Iran (Moghadam and Stern, 2015) to Hasanbag in Iraq (Ali et al., 2013), are related to intra-oceanic subduction in the Neotethyan ocean, similar to volcanic-arc type ophiolites (e.g. Furnes et al., 2020). Eocene and younger ophiolites occur in southeastern Asia in Indonesia (Ishikawa et al., 2007), Philippines (Yumul, 2007), Taiwan (Jahn, 1986) and Japan (Hirano et al., 2003) as well as in western South America, e.g. in Chile (Veloso et al., 2005). Ophiolite studies have shown a wide variety in their lithology and geochemical characteristics (Saccani, 2015). Therefore, not all ophiolites are products of the conventional mid-ocean ridge processes as identified by the Penrose definition (Anonymous, 1972).

The ophiolites in the vast Alpine-Himalayan Orogenic Belt are subdivided into subduction-unrelated and subduction-related type ophiolites in terms of their tectonic setting before becoming incorporated into continental margins (Dilek and Furnes, 2014). The subduction-unrelated ophiolites are subdivided into rift and continental margin types, which show the embryonic stage of ocean crust formation. Continental rifting leads to the onset of seafloor spreading. The subduction-related ophiolites include forearc, backarc to forearc, backarc and volcanic arc ophiolites which all show different geochemical signatures. The backarc and forearc types represent end-members and show low to high and high subduction influence, respectively. The third type of ophiolites are related to plumes which might be part of oceanic plateaus (Dilek and Furnes, 2014).

Within the Alpine-Himalayan Orogenic Belt, the subduction-related ophiolites constitute 76% of the ophiolites and the majority of these are of backarc type (Furnes et al., 2020). Within the Bitlis-Zagros suture zone, the majority of the Neotethyan ophiolites are proposed to have formed in a suprasubduction zone environment, backarc, backarc to forearc and forearc settings (Stern et al., 2012). Mafic and ultramafic rocks are the most abundant components in ophiolites. These are widely used to infer the magmatic events and tectonic histories that occurred in ancient oceanic basins. Different petrological and geochemical characteristics can constrain the nature of the mantle source and provide new insights into the processes that control formation and evolution of mantle-derived melts. These in turn can be used to identify the tectonic environment where they were formed (Piccardo and Guarneri, 2011).

Previous studies on the gabbroic rocks from the Mawat ophiolite (MO) conclude that the gabbros have MORB affinity (Mirza and Ismail, 2007). The metagabbros in the southern part of MO are tholeiitic MORBs formed by partial melting of peridotite (Koyi et al., 2010). Azizi et al. (2013) proposed that the magmatic activity in the MO has some affinity to OIB type and high Mg basalts and conclude that their findings are not consistent with the MORB, island arc or suprasubduction zone as a magma source, but related to plume setting. In this study we describe petrological and geochemical characteristics of the mafic and the ultramafic rocks from the MO. Our findings will be discussed in comparison with previously published data from the MO (Mirza and Ismail, 2007; Koyi et al., 2010; Azizi et al., 2013) and we show that the MO is one of the suprasubduction zone ophiolites within the Alpine- Himalayan Orogenic Belt.

2. Geological Setting

2.1. Regional Geology

The Zagros Orogenic Belt (ZOB) between the Arabian shield and the Sanandaj-Sirjan Zone (SSZ; Fig. 1) contains ophiolitic remnants including Mawat, Penjwen, Bulfat, Pushtashan and Hasanbag in Iraq (Ali et al., 2019; Al Humadi et al., 2019; Ismail et al., 2020) and Piranshah, Sardasht, Marivan and Kermanshah in Iran (Allahyari et al., 2014; Ao et al., 2021; Saccani et al., 2014). They occur

discontinuously along the southern boundary of the SSZ. The ophiolites were emplaced within the forearc accretionary complex of the Eurasia active margin (Zhang et al., 2017). The ZOB formed by long-lasting convergence between the Eurasian and Arabian shields with three major tectonic events: 1) early to late Cretaceous subduction of the Neotethyan oceanic plate beneath the Eurasian continental plate, 2) emplacement of the late Cretaceous Neotethyan ophiolites onto the Arabian continental passive margin, and 3) the Cenozoic collision of the Arabian and Eurasian continental plates (Moghadam et al., 2019).

The ZOB is composed of three tectonic subdivisions: (a) the Zagros Fold-Thrust Belt is ~ 2000 km long and is folded and shortened after the Miocene. The belt consists of 12-13 km thick Cambrian to Quaternary sediment cover on the Arabian plate passive margin (Agard et al., 2011), (b) the Sanandaj-Sirjan Zone represents a micro-continent rifted from the Arabian plate in the late Permian and accreted to the southern margin of Eurasia in the late Triassic (Agard et al., 2011), and (c) the Urumieh-Dokhtar Magmatic assemblage is 150 km wide and a distinctively linear and voluminous magmatic arc of the Tertiary age (Omrani, 2008) (Fig. 1).

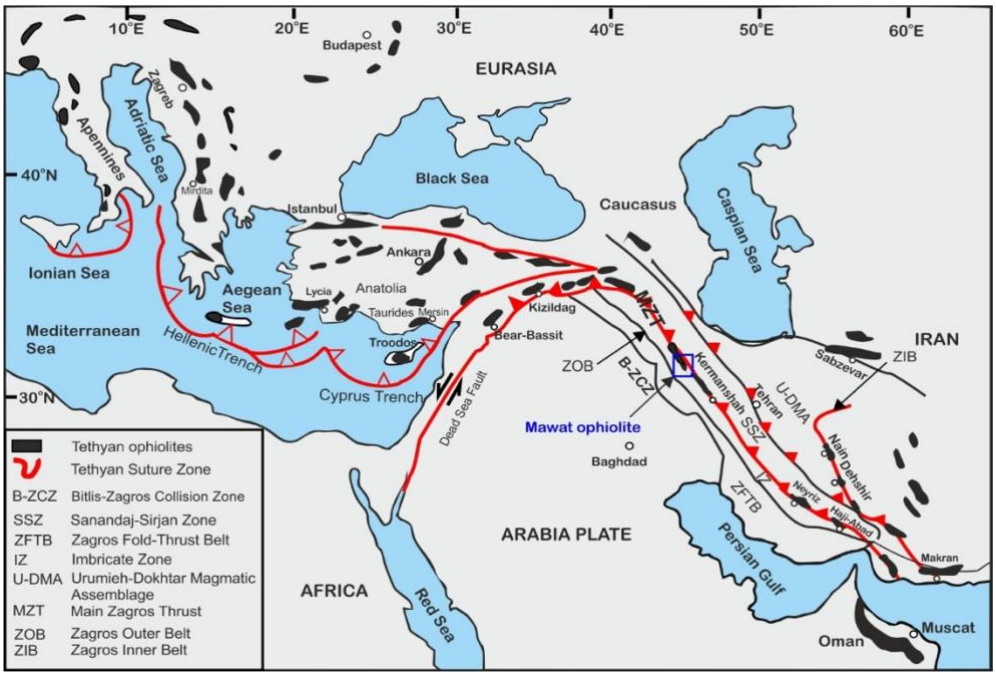

Fig. 1. Distribution of Tethyan ophiolites (modified from Dilek et al., 2007). The tectonic units and boundaries of the Zagros Orogenic Belt are modified from Alavi (2007).

The Iraqi Zagros Suture Zone (IZSZ) is subdivided into three tectonic sub-zones (Jassim and Goff, 2006): (1) the Qulqula-Khwakurk is the southern segments of the Neotethyan ocean obducted onto the Arabian plate in the late Cretaceous age, (2) the Penjwen-Walash is the central part of the Neotethyan ocean, and (3) the Shalair is a part of the SSZ in Iran (Stöcklin, 1968) (Fig. 2). The ophiolites of Iraq occur within the Penjwen-Walash sub-zone, which consists of three thrust sheets: (1) the lower Naopurdan, (2) the middle Walash and (3) the upper Qandil. The lower and middle sheets are combined into one group called the Walash-Naopurdan group, which is a volcano-sedimentary sequence containing basalt, diabase, andesite, tuff, limestone and chert. The ^{40}Ar-^{39}Ar dating of the volcanic rocks indicates ages between 43 and 24 Ma (Ali et al., 2013). The Cenozoic ophiolites occur as incomplete fragments and poorly preserved mélange-like assemblages within the Eocene-Oligocene Walash-Naopurdan group. These are the Rayat and Qalander ophiolites (Arai et al., 2006) (Fig. 2). The upper Qandil sheet is characterized by the Cretaceous ophiolites including Penjwen, Mawat, Bulfat and

Pushtashan (Ismail et al., 2017; Al Humadi et al., 2019). The Qandil assemblages are thrusted over the Qulqula-Khwakurk sub-zone (Jassim and Goff, 2006).

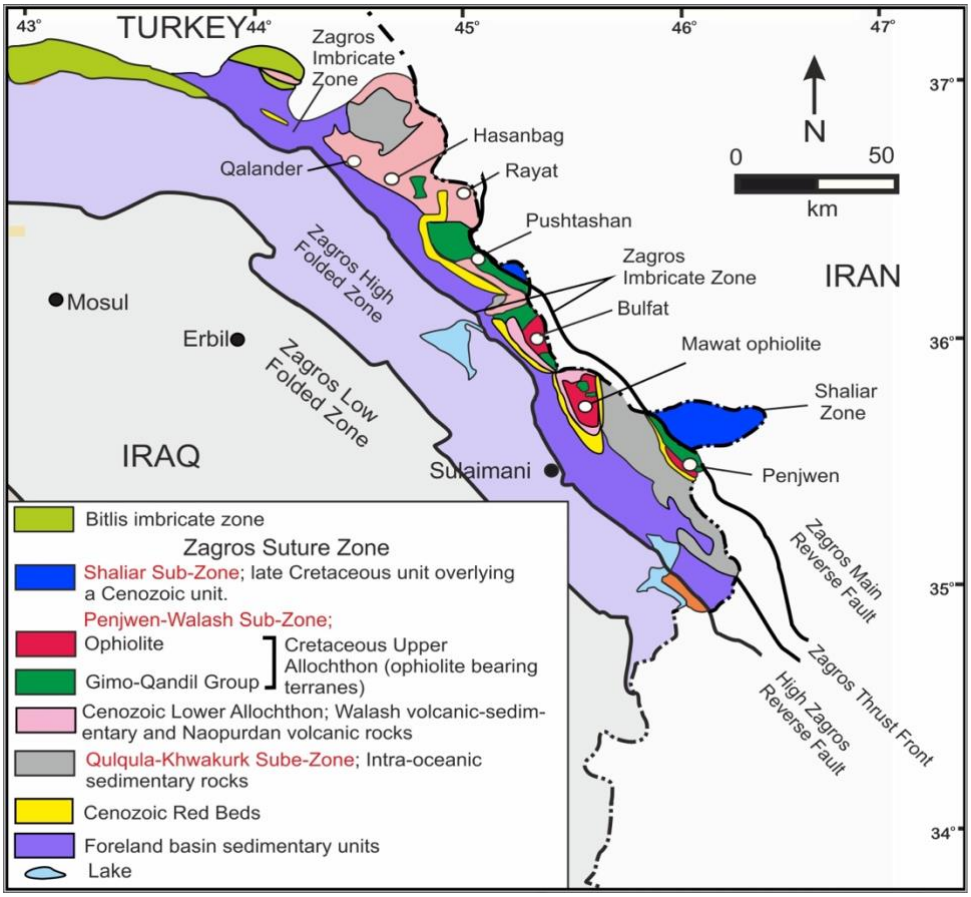

Fig. 2. Regional tectonic map of northeastern Iraq showing the major tectonic subdivisions, modified from Al-Kadhimi et al. (1996). Tectonic zones and boundaries modified from Al-Qayim et al., (2012) Zagros Suture Zone.

2.2. Geology of the Mawat Ophiolite

The MO crops out over ~ 250 km^2 in an elevated and rough topographic area northeast of the city of Sulaimani in northeastern Iraq and lies between two thrust sheets (Figs. 2 and 3). The eastern sheet is the Walash group, which comprises metamorphosed red shales, limestones and mafic volcanic rocks (Ali et al., 2013). The western sheet is the Naopurdan group of volcano-sedimentary successions (Ali et al., 2013). The MO comprises mantle and crustal sections: the mantle peridotites include serpentinized harzburgitess, dunite, chromitites and minor lherzolites. Numerous pyroxenite dykes intruded the mantle peridotite and dunites (Fig. 4c, d and g). The crustal section makes two-thirds of the exposed ophiolite consisting of layered and amphibole-rich gabbros intruded by minor diorite and diabase dykes (Jassim and Goff, 2006). The crustal section is lacking the sheeted dykes. The gabbro is the main component and form most of the central part of the MO (Jassim, 1973) and covers an area about 170 km^2 (Fig. 3). The layered gabbro, which consists of alternating plagioclase-rich and pyroxene-rich bands, is the main type surrounded by the sheared gabbro and ultramafic rocks in the east and by metabasalts and amphibolites in the west, southwest and south (Buda and Al-Hashimi, 1977).

The pegmatitic gabbro occurs as lenses within the layered gabbro in the western, northern, and southern parts (Jassim, 1973). In the east, the pegmatitic gabbro occurs within the ultramafic rocks (Jassim and Goff, 2006; Al Humadi et al., 2019).

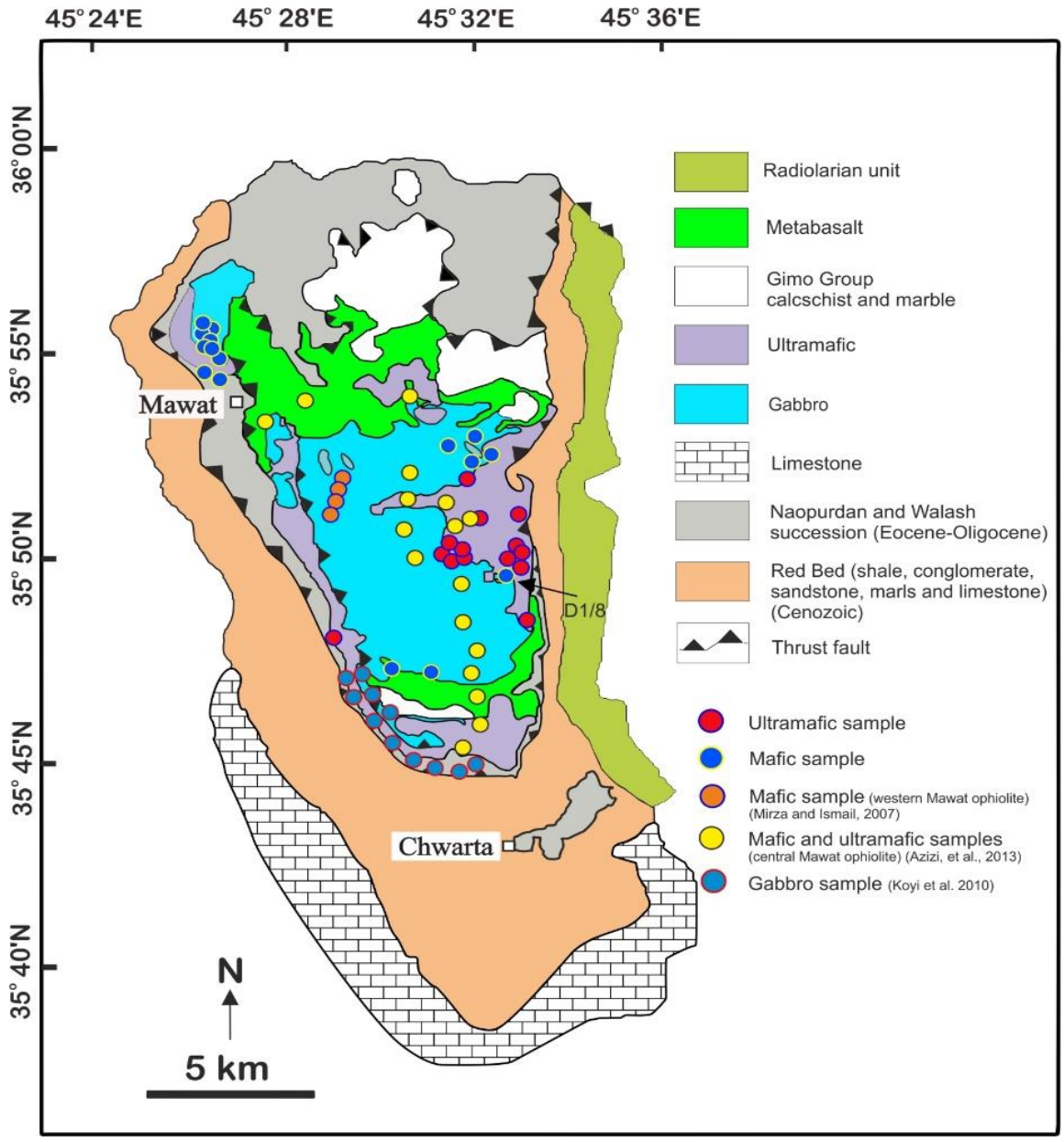

Fig. 3. Simplified geological map of the Mawat ophiolite, modified from Aziz (2008). The samples of this study and the comparison samples are indicated.

The plagiogranite/tonalite dykes intruded the gabbros in the west (Mirza and Ismail, 2007) and leucogranites/granites intruded the mantle peridotite in the central MO (Mohammad et al., 2014). These two types of felsic dykes intruded the mantle section in the eastern part (Al Humadi et al., 2021). The volcanic rocks occur in two groups: the lower one is the metavolcanic Mawat group and the upper one is the volcano-sedimentary Gimo group. The volcanic rocks are exposed in the northern and southern parts and are composed of alternating white siliceous carbonate and dark calcschist with thin metavolcanic interlayers (Fig. 3). The contacts between the layered gabbro, peridotite and volcanic rocks are thrust faults (Mirza and Ismail, 2007). The Mawat group is overlain by the Gimo group and both groups underwent low-grade metamorphism (Jassim and Goff, 2006).

The radiometric dating of the felsic rocks from the MO yielded the crystallization ages of 94.6 ± 1.2 Ma (U-Pb monazite in a felsic dyke; Al Humadi et al., 2019), 96.8 ± 6.0 Ma (U-Pb zircon in a granite; Mohammad and Cornell, 2017) and 93.4 ± 1.8 Ma (Rb/Sr mineral isochron of a granitic dyke; Azizi et al., 2013). The pegmatitic gabbro in the eastern part of the MO yielded an age of 81 ± 3 Ma (zircon: Al Humadi et al., 2019).

3. Materials and Methods

Sixteen mafic and sixteen ultramafic whole-rock analyses for major and trace elements were carried out at Acme Analytical Laboratories Ltd. (Acme) in Vancouver, Canada. The samples were pulverised in a mild steel swing mill and after the $LiBO_2$ fusion and HNO_3 dilution, the major elements were analysed by inductively coupled plasma-emission spectrometry (ICP-OES). The trace elements were analysed by inductively coupled plasma-mass spectrometry (ICP-MS). The analytical precision is 1-5% for the major oxides and ±10% for the other elements. Due to the extremely low concentrations of many elements (below detection limits), the second batch of six mafic and seven ultramafic samples were re-analysed with a method of lower detection limits. These samples were analysed in Acme Analytical Laboratories Ltd. (Acme) in Perth, Australia. The samples were crushed and then pulverised in a mild steel swing mill and cast using a 66:34 flux with 4% $LiNO_3$ added to form glass bead. The major elements were analysed by X-Ray Fluorescence Spectrometry (XRF) on oven dry (105°C) sample. The trace elements were analysed by Fused Bead for Laser Ablation inductively coupled plasma-mass spectrometry (ICP-MS). In this study, the analysed data from the first batch were used. In cases where these analyses were below detection limit, the analyses from the second batch were used which are above detection limit. The analysed data are presented in the Appendix. The geochemical data were plotted with the GCDKit software (Janoušek et al., 2006). Thirty-one mafic and ultramafic samples from published sources were used for the comparison and discussion. They include four gabbro samples from the western part of the MO (Mirza and Ismail, 2007), fourteen mafic and ultramafic samples from the central part of the MO (Azizi et al., 2013) and eleven mafic samples from the southern part of the MO (Koyi et al., 2010).

4. Results

4.1. Petrography

4.1.1. Mafic rocks (basalts and gabbros)

The petrographic study for the mafic rocks is carried out on sixteen samples. The basalts are predominantly aphyric or micro porphyric with equigranular to intergranular groundmass. They are composed of subhedral plagioclase and clinopyroxene ± orthopyroxene in a groundmass of chlorite, epidote, and opaque minerals. The plagioclase is partially altered to sericite, calcite and epidote minerals. The pyroxene is altered to secondary amphibole and chlorite. Small amygdules are filled with quartz or calcite and chlorite (Fig 5a).

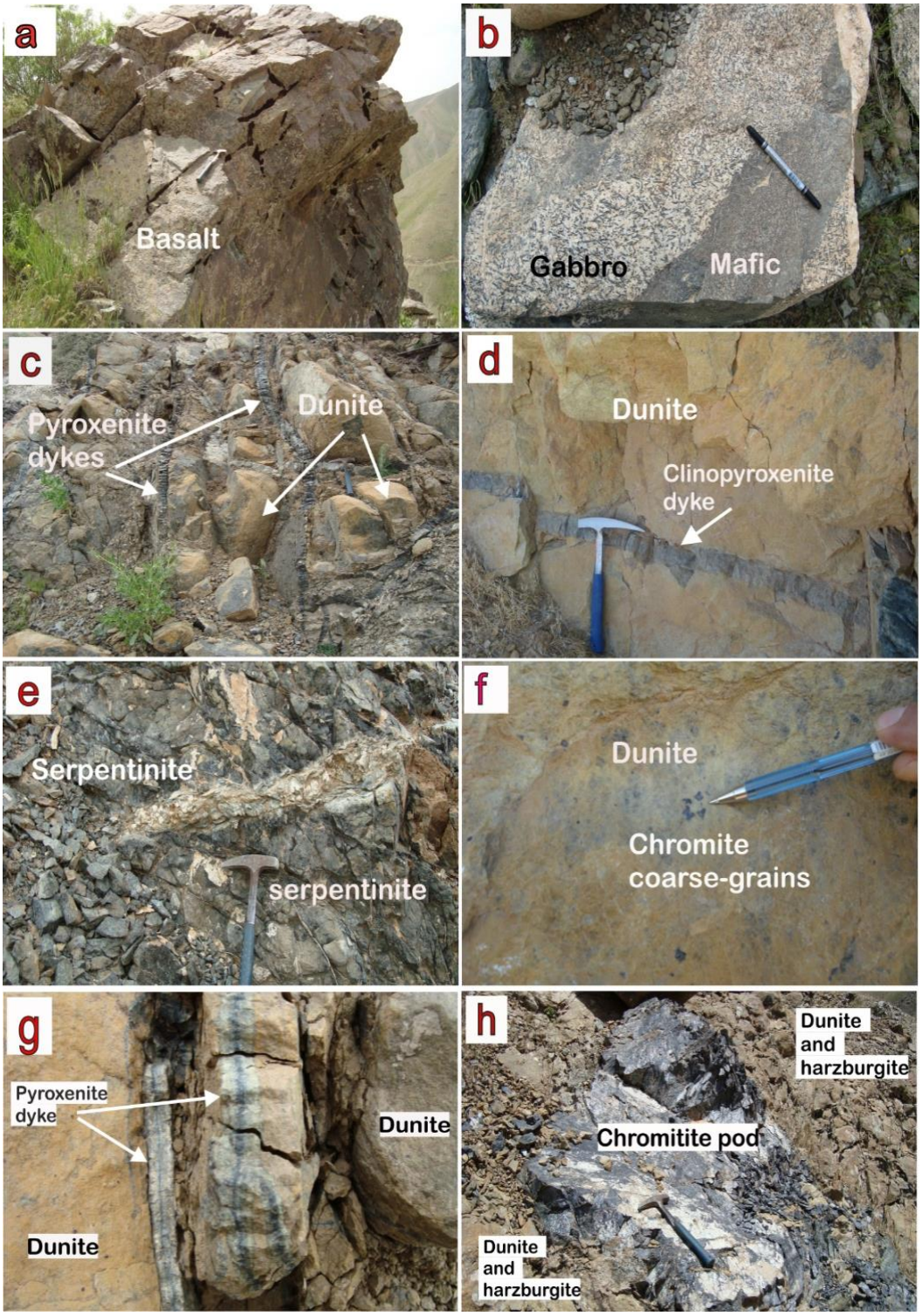

Fig. 4. Field photographs of the mafic and ultramafic rocks: (a) basalts, (b) pegmatite gabbro, (c) dunite rock of ellipsoidal shape intruded by pyroxenite dykes hosted by peridotite rocks, (d) a massive block of dunite intruded by pyroxenite dyke, (e) serpentinite, (f) chromite coarse-grain within a massive dunite, (g) pyroxenite dykes, and (h) chromitite pod enclosed by dunite and harzburgite host rock.

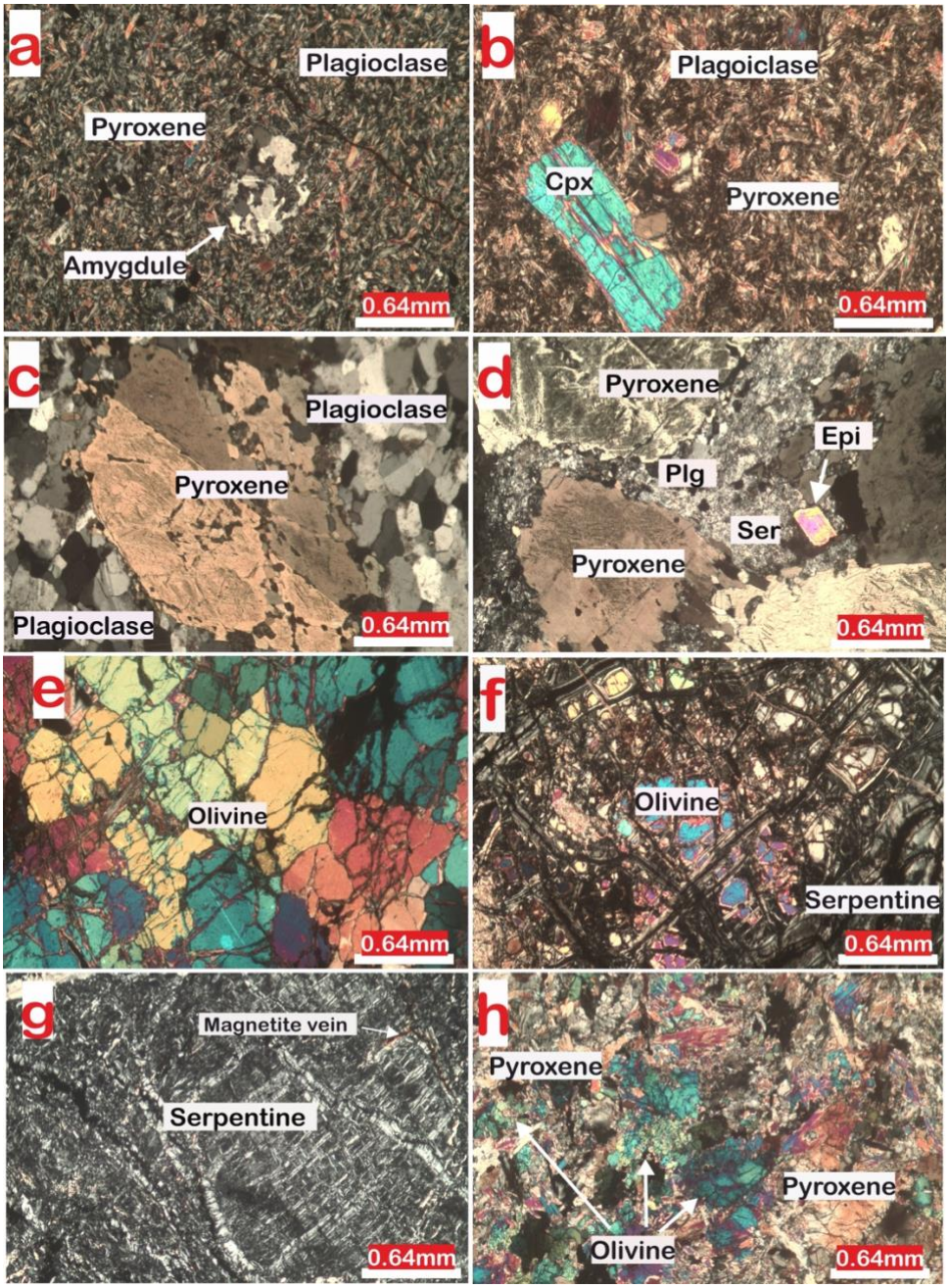

Fig. 5. Photomicrographs (cross-polarized light) of mafic and ultramafic thin sections, (a) basalt sample showing aphyric and micro-porphyric and equigranular textures, composed of fine-grained plagioclase and pyroxene with amygdule structure, (b) basaltic sample is porphyric with equigranular to intergranular groundmass texture composed of subhedral plagioclase and clinopyroxene ± orthopyroxene, (c) and (d) gabbroic samples are medium to coarse-grained of porphyric, poikilitic, and subophitic textures, plagioclase and pyroxene are the main components, (e) massive dunite sample showing the xenomorphic granular texture of fresh olivine grains, (f) serpentinized peridotite sample showing serpentines replacing olivine and display mesh texture, (g) serpentinite sample shows pseudomorphic texture, the olivine completely replaced by serpentines and exemplified by mesh texture, (h**)** pyroxenite dyke composed of fine to coarse-grained of pyroxene and olivine. Plg = Plagioclase; Epi = Epidote; Ser = Sericite; Cpx = Clinopyroxene.

The layered gabbro is medium to coarse-grained with hypidiomorphic granular texture and composed of plagioclase, pyroxene, chlorite and opaque minerals. Accessory minerals are quartz,

chlorite, magnetite and ilmenite. The plagioclase is partly altered to sericite. The pyroxene is partially or completely altered to secondary amphibole (Fig 5c) and chlorite. The pegmatitic gabbro is medium to coarse-grained and some crystals are up to 1.5 cm (Fig. 4b). The samples display porphyric, poikilitic and sub-ophitic textures. The plagioclase is partly to completely altered to sericite. The pyroxene is partially or completely altered to amphibole. The epidote, chlorite, opaque minerals and undefined minerals are the accessories (Fig. 5d).

4.1.2. Ultramafic rocks

The petrographic study for the ultramafic samples is carried out on 16 samples. The rocks are most common in the eastern and less abundant in the southern and northern parts of the MO (Jassim 1972). The studied ultramafic rocks fall into two group: the first group comprises dunites and serpentinites and the second group pyroxenite dykes. The dunites occur in two types: the first is irregular, ellipsoidal type and the second is massive block type. The first irregular type is of various sizes and occur within the peridotite host rocks (Fig. 4c). Olivine is dark green to black in colour in the hand samples, meanwhile it is microscopically partly to completely altered to serpentine and magnetite along the fractures and grains rims to produce a mesh texture (Fig. 5g). Irregularly shaped fine-grained spinel occurs disseminated in the dunite. Commonly, the dunite and peridotite host chromitite pods in the Ser Shiw valley (Fig. 4h). The dunite has a graded contact relation with the chromitite pods. The spheroidal dunite bodies and the peridotite were intruded by pyroxenite dykes and their contact relations with the dykes are sharp (Fig. 4c and g). Mohammad (2020) classifies the dunite as a tectonite dunite.

The second type of dunite is massive blocks (Fig. 4d and f). In the thin section, the samples show xenomorphic granular textures and are composed of fresh olivine with accessory chromian spinel and pyroxene relics (Fig. 5e). The olivine is anhedral and > 0.3 mm in size. Small amount of serpentine occurs in the olivine fractures. The euhedral to subhedral black chromian spinel crystals are up to 1.5 cm in diametre in the lower part of the dunite massive block (Fig. 4f). This type of dunite is a cumulate (Mohammad, 2020). In some samples, the olivine has survived in the core of the mesh (Fig. 5f). Some serpentinite samples are composed of primary olivine, pyroxene, serpentine and chromian spinel and talc as well as opaque minerals observed within the mesh texture of olivine pseudomorphs. The fine-grained grey pyroxenites occur as 5 to 15 cm thick dykes and sills intruding the ultramafic rocks (Fig. 5c). The 2-5 cm light grey margin in some pyroxenites gradually become dark toward the central part (Fig. 4d and g). The margins have sharp contacts with dunite and peridotite host rocks. The dykes are composed of pyroxenes partially altered to secondary amphibole and minor olivine, plagioclase and Cr-spinel along the cleavage (Fig. 5h).

4.2. Geochemistry

4.2.1. Mafic rocks (basalts and gabbros)

Field observations and petrographic study show that certain samples underwent alterations. The loss-on-ignition (LOI) values of the basalts and gabbros range from 0.3-5.9 % and 2.4 -1.2 %, respectively. The basalts are characterized by moderate to high SiO_2 (44.1- 60.24 wt. %) and MgO (5.44-16.84 wt. %). Fe_2O_3 (7.31-16.76 wt. %), Al_2O_3 (11.43-17.78 wt. %), and CaO (2.55- 13.45 Wt. %), but low in TiO_2 (0.20-0.86 wt. %) and P_2O_5 0.01-0.04 wt. %. The basalts have Mg# values ranging from 63.4 to 76.9 except for one sample with Mg of 39.1 (Table 1).

Table 1. The whole rock geochemistry for the basaltic rocks from the Mawat ophiolite.

Samples	D1/8	D1/13B	D1/16	D2/1	D2/2A	D2/2B	D2/3A	D2/3B	D2/3C	D2/3D	D2/3E	D2/3F
N-Cood	35° 54. 42'	35° 47. 12'	35° 47. 11'	35° 55. 04'	35° 55. 08'	35° 55. 09'	35° 54. 58'	35° 54. 58'	35° 54. 58'	35° 54. 58'	35° 54. 58'	35° 54. 58'
E-Cood	45° 31. 48'	45° 31. 10'	45° 30. 41'	45° 26. 38'	45° 26. 42'	45° 26. 40'	45° 26. 28'	45° 26. 28'	45° 26. 28'	45° 26. 28'	45° 26. 28'	45° 26. 28'
Locality	Kanishakra	Waraz	Waraz	Spaidra	Spaidra	Spaidra	Spaidra body	Spaidra	Spaidra	Spaidra	Spaidra	Spaidra
Rock type	Picro-basalt	Basaltic andesite	Basaltic andesite	Basalt	Basalt	Basaltic andesite	Basaltic andesite	Andesite	Basaltic andesite	Basaltic andesite	Basalt	Basaltic andesite
SiO2	44.1	55.26	55.54	46.6	48.94	53.27	53	60.24	53.02	51.89	47.97	52.14
Al2O3	17.78	11.43	12.16	12.9	16.05	12.35	10.11	13.12	13.84	12.21	12.14	15.43
Fe2O3	16.76	8.8	9.43	10.51	10.96	9.23	8.77	7.31	8.77	8.89	9.92	9.67
MgO	5.44	10.64	8.47	16.84	9.6	8.22	14.81	8.85	10.01	13.19	16.36	10.3
CaO	13.45	9.94	8.97	5.01	7.82	10.55	6.14	2.55	5.94	5.14	5.05	6.1
Na2O	0.25	0.79	4.29	1.61	3.08	3.8	1.7	3.57	3.88	2.63	1.46	1.39
K2O	0.03	0.06	0.12	0.1	0.42	0.18	0.05	0.12	0.68	0.15	0.1	0.47
TiO2	0.86	0.2	0.28	0.31	0.41	0.28	0.24	0.31	0.24	0.28	0.29	0.25
P2O5	0.02	0.02	0.02	0.03	0.03	0.03	0.02	0.04	0.01	0.02	0.02	0.01
MnO	0.19	0.14	0.15	0.34	0.12	0.16	0.36	0.1	0.17	0.29	0.35	0.08
Cr2O3	0.003	0.088	0.119	0.177	0.038	0.071	0.128	0.01	0.03	0.061	0.178	0.023
Sc	46	36	43	44	69	41	41	34	46	46	42	43
LOI	0.9	2.5	0.3	5.3	2.4	1.7	4.5	3.7	3.3	5.1	5.9	4
Sum	99.77	99.88	99.88	99.81	99.85	99.89	99.85	99.87	99.87	99.83	99.81	99.9
Ba	3	6	24	10	55	21	12	25	40	49	12	24
Be	<0.2	1	<1	0.4	<0.2	2	<1	<1	<0.2	0.4	<1	<0.2
Co	43.8	46	48	39.5	41.1	36.6	27.7	32.2	30.6	33.2	39.4	39
Cs	0.4	<0.1	0.1	0.2	0.3	0.4	<0.1	<0.1	0.1	0.3	0.2	0.8
Ga	21	8.8	9.4	10.4	13	9.4	8.5	8.8	9.7	8.9	10.9	11.3
Hf	0.2	0.3	0.3	0.4	0.4	0.5	0.2	0.4	0.3	0.2	0.3	0.3
Nb	0.15	<0.1	0.1	0.31	0.79	<0.1	0.1	<0.1	0.43	0.26	<0.1	0.28
Rb	0.4	0.5	1.9	0.8	5.3	2.5	0.4	0.9	5.1	1.3	1	7.9
Sn	0.8	<1	<1	0.6	0.6	<1	<1	<1	0.6	<0.2	<1	0.4
Sr	219.6	45.1	88.7	28.4	140.1	61	34.6	64.9	74.2	53.3	30.9	78.5
Ta	0.01	<0.1	<0.1	0.01	0.04	<0.1	<0.1	<0.1	<0.01	<0.01	<0.1	<0.01
Th	<0.01	<0.2	<0.2	0.18	0.32	<0.2	<0.2	<0.2	0.15	0.11	<0.2	0.14
U	0.05	<0.1	<0.1	0.19	0.16	0.2	0.3	0.2	0.08	0.09	0.2	0.07
V	913	209	256	255	324	300	257	176	273	261	246	219
W	<0.5	0.7	<0.5	<0.5	<0.5	<0.5	<0.5	<0.5	<0.5	<0.5	<0.5	<0.5
Zr	5.5	6.1	9.2	9.3	11.5	8.9	7.5	10.1	7.4	5.7	9.3	6.2
Y	4.8	5.7	6.1	7.7	9	8.7	8.5	7.1	7.2	7.9	8.9	4.2
La	0.5	0.5	0.4	0.4	0.5	0.6	0.4	0.5	0.6	0.5	0.6	0.3
Ce	1	0.8	0.8	1	1.8	1.3	1	0.7	1.1	0.7	1.2	0.6
Pr	0.12	0.14	0.09	0.19	0.26	0.2	0.18	0.12	0.15	0.12	0.22	0.06
Nd	0.6	0.7	0.5	1.2	1.2	1	1.2	1	0.8	0.8	1.6	0.5
Sm	0.37	0.35	0.4	0.6	0.57	0.5	0.72	0.37	0.38	0.41	0.42	0.3
Eu	0.18	0.18	0.18	0.21	0.22	0.2	0.22	0.16	0.16	0.19	0.24	0.14
Gd	0.55	0.66	0.7	0.84	1.09	0.88	0.95	0.78	0.66	0.79	0.97	0.55
Tb	0.12	0.15	0.15	0.18	0.24	0.19	0.22	0.15	0.16	0.18	0.21	0.11
Dy	0.85	1.12	1.12	1.18	1.69	1.33	1.5	1.14	1.09	1.28	1.5	0.62
Ho	0.19	0.22	0.26	0.31	0.42	0.28	0.32	0.27	0.25	0.34	0.36	0.15
Er	0.61	0.71	0.64	0.92	1.2	0.96	1.11	0.9	0.79	1.06	1.17	0.51
Tm	0.1	0.11	0.13	0.16	0.21	0.13	0.18	0.15	0.14	0.16	0.16	0.09
Yb	0.69	0.83	0.74	1.16	1.45	0.99	1.24	0.88	0.98	1.25	1.07	0.71
Lu	0.09	0.12	0.13	0.17	0.27	0.14	0.21	0.15	0.18	0.19	0.18	0.09
TOT/C	<0.02	<0.02	<0.02	<0.02	<0.02	0.26	<0.02	<0.02	<0.02	0.03	<0.02	0.02
TOT/S	0.26	<0.02	<0.02	<0.02	<0.02	<0.02	<0.02	1.11	<0.02	0.82	<0.02	<0.02
Mo	1.4	0.5	0.3	0.3	<0.2	0.5	0.6	1.3	0.2	0.6	0.1	0.3
Cu	123.3	161.4	42	271.2	158	29.6	68.5	54.7	92.2	223.6	215.6	4.9
Pb	2	0.4	0.7	3	0.7	0.3	2.6	23.1	6.9	5.3	4.1	0.7
Zn	24	19	6	394	30	7	161	182	76	242	351	42
Ni	11.8	69.7	23.1	246	55.3	15.9	119.6	50.2	39.5	75.7	250.2	42.7
Cr	20.526	602.096	814.198	1211.034	259.996	485.782	875.776	68.42	205.26	417.362	1217.876	157.366
As	0.6	<0.5	0.5	9.8	0.7	<0.5	13.4	21.4	5.8	9.9	6.5	0.6
Cd	<0.1	<0.1	<0.1	<0.1	<0.1	<0.1	0.1	0.7	0.1	0.2	<0.1	<0.1
Sb	<0.1	<0.1	<0.1	<0.1	0.2	<0.1	0.1	<0.1	0.4	0.4	<0.1	0.3
Bi	0.06	<0.1	<0.1	<0.1	0.1	<0.1	0.2	0.1	0.04	0.1	0.1	0.04
Ag	<0.1	<0.1	<0.1	<0.1	<0.1	<0.1	0.2	0.2	0.2	0.2	<0.1	<0.1
Au	1.6	2.9	1.2	2.1	3.5	1.4	11.3	15.9	1.5	6.1	1.5	<0.5
Hg	<0.01	<0.01	<0.01	<0.01	<0.01	<0.01	<0.01	<0.01	<0.01	<0.01	<0.01	<0.01
Tl	<0.1	<0.1	<0.1	<0.1	<0.1	<0.1	<0.1	<0.1	<0.1	<0.1	<0.1	<0.1
Se	<0.5	<0.5	<0.5	<0.5	<0.5	<0.5	0.9	7	<0.5	1	<0.5	<0.5
Mg#	39.1	70.5	64	76	63.4	63.8	76.9	70.5	69.3	74.6	76.5	67.8
LaN/YbN	0.49	0.41	0.37	0.23	0.23	0.41	0.22	0.39	0.42	0.27	0.38	0.29
LaN/SmN	0.85	0.9	0.63	0.42	0.55	0.75	0.35	0.85	0.99	0.76	0.9	0.63
CeN/YbN	0.38	0.25	0.28	0.23	0.33	0.35	0.21	0.21	0.3	0.15	0.3	0.22
CeN/SmN	0.66	0.55	0.48	0.4	0.77	0.63	0.34	0.46	0.7	0.41	0.69	0.48
REE SUM	5.97	6.59	6.24	8.52	11.12	8.7	9.45	7.27	7.44	7.97	9.9	4.73
ThN	0.04	0.83	0.83	1.5	2.67	0.83	0.83	0.83	1.25	0.92	0.83	1.17
NbN	0.06	0.02	0.04	0.13	0.34	0.02	0.04	0.02	0.18	0.11	0.02	0.12

The gabbros have moderate amounts of SiO_2 (44.08-50.83 wt %), Al_2O_3 (11.66-18.44 wt. %), MgO (3.71-14.52 wt. %), Fe_2O_3 (9.87-11.56 wt. %) and CaO (8.08-11.97 wt. %) and moderate to high

amounts of TiO_2 (0.82-1.64 wt. %). They contain 0.02-0.63 wt. % P_2O_5, 2.17- 5.87 wt. % Na_2O and 0.2-0.29 wt %. K_2O. The Mg# of the gabbros range from 42.6 to 71.8 (Table 2). The major element diagrams are shown in Fig. 6.

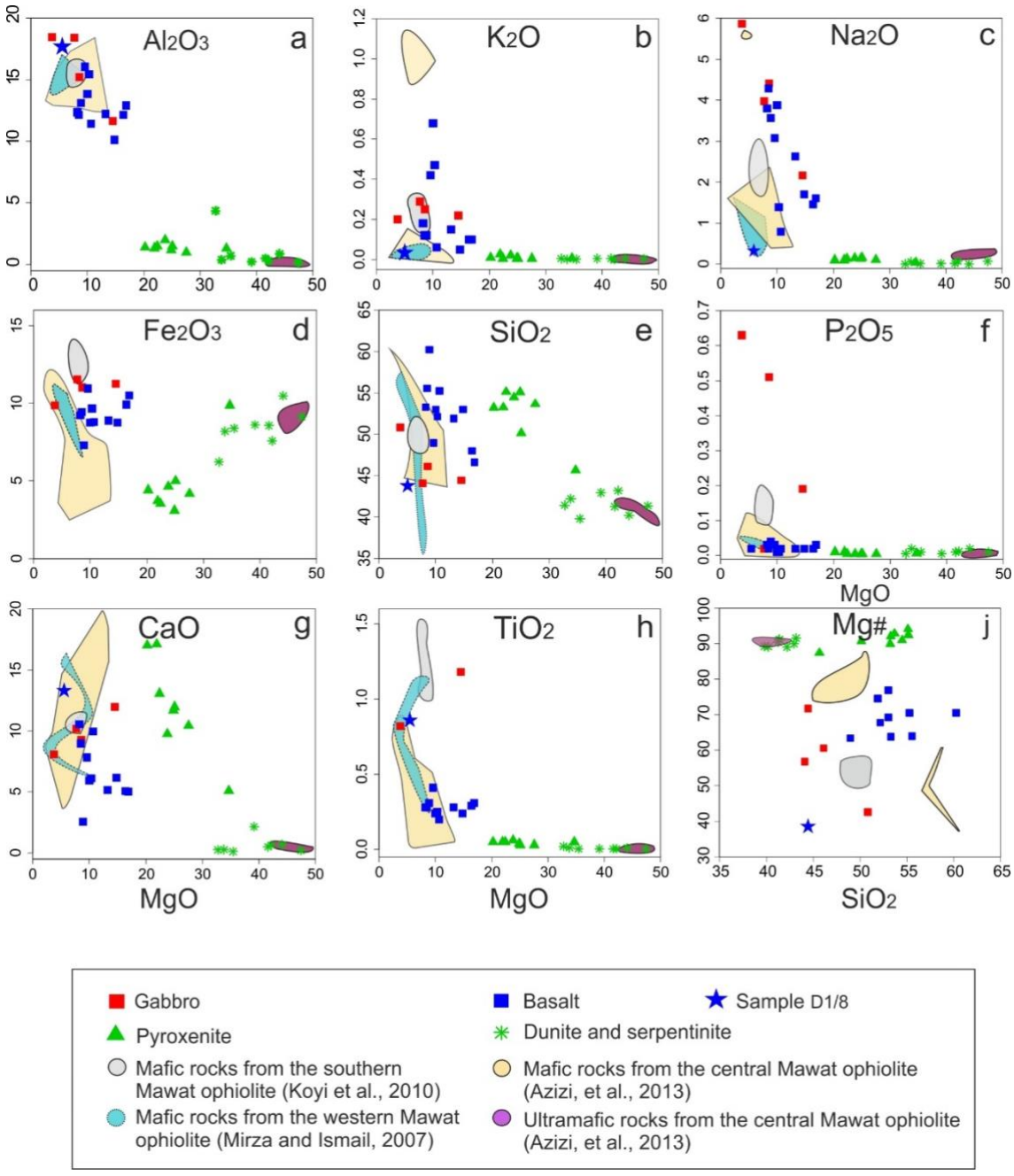

Fig. 6. Selected major element vs. MgO (a-h) and Mg vs. SiO_2 (j) diagrams. Mg = (100*MgO/ (FeO_t+MgO)). All values are in weight %, except Mg.

The TAS diagram shows that the basaltic samples mostly fall in the basaltic andesite field and few of them in the basalt field. The gabbroic samples fall in the basalt field with the exception of one sample which falls within the basaltic trachyandesite field (Fig. 7a). The high SiO_2 (51.89 to 60.24 wt. %) and and MgO (8.22 to 16.84 wt. %) combined with low TiO_2 (0.2 to 0.41wt. %) relate them to boninites (Fig. 8). One of the samples (sample D1/8) differs in many ways from the others. It is the only mafic sample that comes from eastern Mawat, surrounded by ultramafic rocks (Fig. 3).

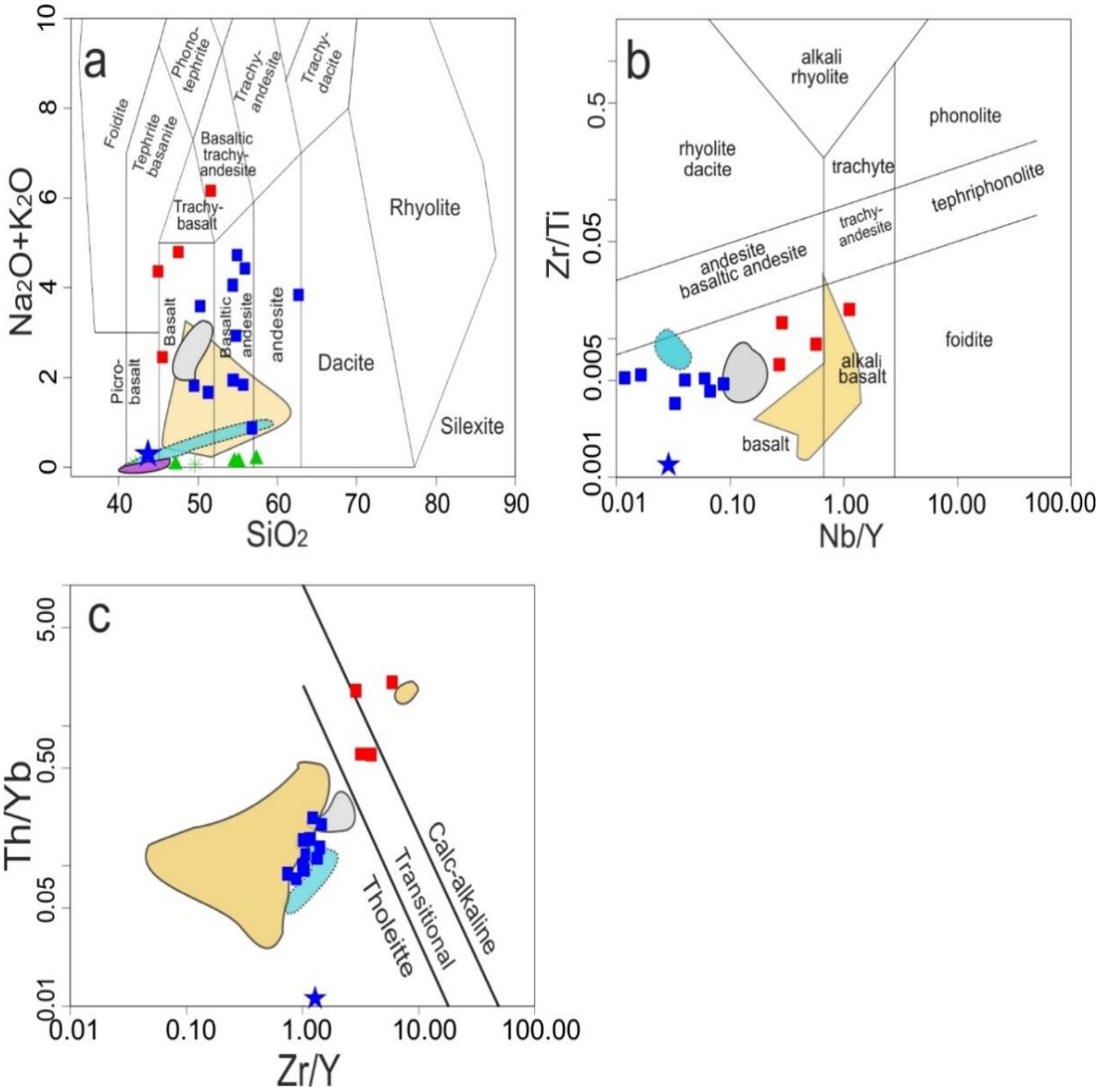

Fig. 7. Classification diagrams: a) Total Alkali vs. Silica (TAS) diagram (Middlemost, 1994), b) Nb/Y vs. Zr/Ti (modified by Pearce, 1996), c) Zr/Y vs. Th/Yb (Ross and Bedard, 2009) diagram. Symbols as in Fig. 6

In the immobile element Nb/Y vs. Zr/Ti diagram, the basaltic and gabbroic samples fall in the basalt field except for one gabbroic sample that plots in the alkali-basalt field (Fig. 7b). The Zr/Y vs Th/Yb diagram shows that the studied gabbros are calc-alkaline unlike all the other mafic rocks which are tholeiitic (Fig. 7c). The basalts have low ΣREE contents (4.73-11.12 ppm) with LREE-depletion relative to HREE [$(La/Yb)_N$ 0.22-0.49] and indistinct Eu-anomaly (Fig. 9a). In the multi-elements diagram based on the N-MORB normalized immobile elements, the basaltic samples are extremely depleted in the LILEs and HFS elements Nb, Zr, Ta and Th. They plot below the N-MORB reference line (Fig 9b). In the N-MORB-normalized multi-elements diagram, the basaltic samples show distinct humps for U, K, Pb and Sr, and troughs for Nb, Ce, and Pr (Fig. 9d). The basaltic samples show very

low concentrations of Nb (<0.79 ppm), Ta (<0.1ppm), Th (<0.32 ppm), Zr (< 11.5 ppm) and Y (< 8.9 ppm) (Table 1).

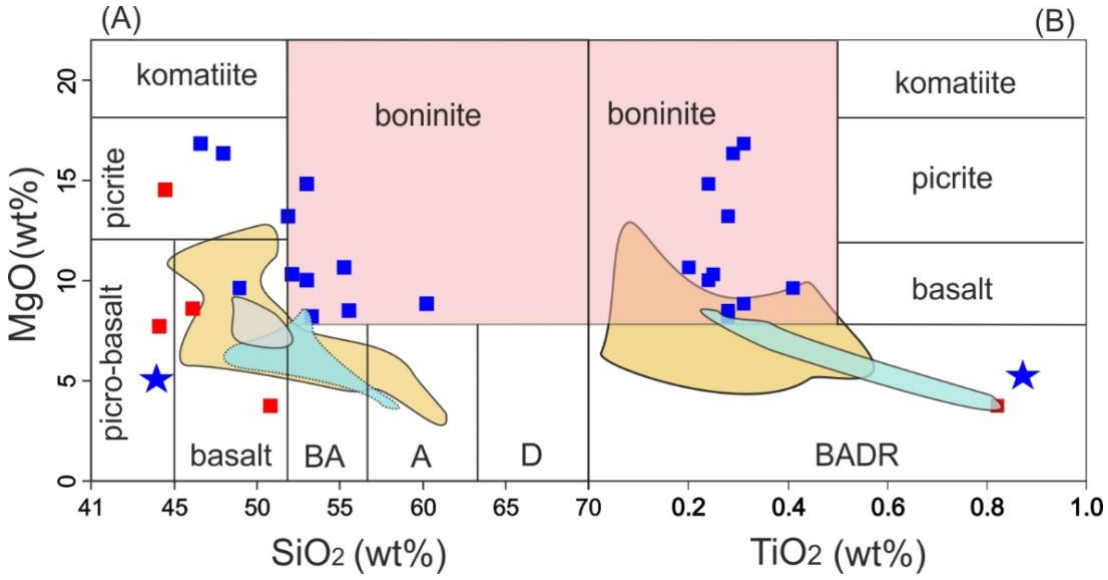

Fig. 8. Boninite classification diagram after Pearce and Arculus (2021), based on Le Bas et al. (2000). a) SiO_2 vs MgO, b) TiO_2 vs MgO. BA= basaltic andesite; A= andesite; D = dacite; BADR = basalt-andesite-dacite-rhyolite.

The ΣREE of the gabbros are 62.8-158.6 ppm, much higher than those of the basalts (4.7-11.1 ppm; Table 1). Their chondrite-normalized REE patterns are different and the gabbros have a negative straight trend [$(La/Yb)_N$ = 3.96-10.34] from the LREE to HREE, while the basalts have a positive trend. Neither of them show visible Eu-anomaly (Fig. 9a).

The N-MORB-normalized immobile multi-element diagram shows that the gabbroic samples fall parallel and partly above the N-MORB reference line (Fig. 9b). In the N-MORB-normalized diagram, the gabbros show LILE enrichment except for some samples which show depletion in Rb and K. The HFSEs show a depletion in Nb, Zr and Ti (Fig. 9c).

4.2.2. Ultramafic rocks

The whole-rock analyses for the dunite, serpentinite and pyroxenite groups are presented in Table.3. The range of major elements in the dunites and serpentinites are 39.78 - 43.18 wt. % SiO_2, 23.74 - 47.41 wt. % MgO, 6.23 - 10.49 wt. % Fe_2O_3, 0.15 - 4.35 wt. % Al_2O_3, < 0.02 wt. % TiO_2, < 0.01 wt. % K_2O, < 0.07 wt. % Na_2O, 0.1 – 2.14 wt. % CaO and 0.34 - 1.54 wt. % Cr_2O_3 (Table 3).

The pyroxenite dykes are rich in SiO_2 (50.13 - 55.14 wt. %) and CaO (9.76-17.12 wt. %) and poor in MgO (20.24 - 27.56 wt. %), Fe_2O_3 (3.09 - 5.01 wt. %), and Cr_2O_3 (0.33 - 0.54 wt. %) compared to the dunites and serpentinites. The pyroxenites have low content of Al_2O_3 (0.97 - 1.97 wt. %) and extremely low TiO_2 (<0.06 wt. %), K_2O (< 0.025 wt. %) and Na_2O (< 0.1 wt. %) contents. The major elements of the ultramafic rocks show variable correlation with the MgO. Al_2O_3, SiO_2 and CaO show negative correlations (Figs. 6a, e, and g), while Fe_2O_3 shows positive correlations with increasing MgO (Fig. 6d). Mg# values in the ultramafics range from 87.4 - 94.1 (Fig. 6i).

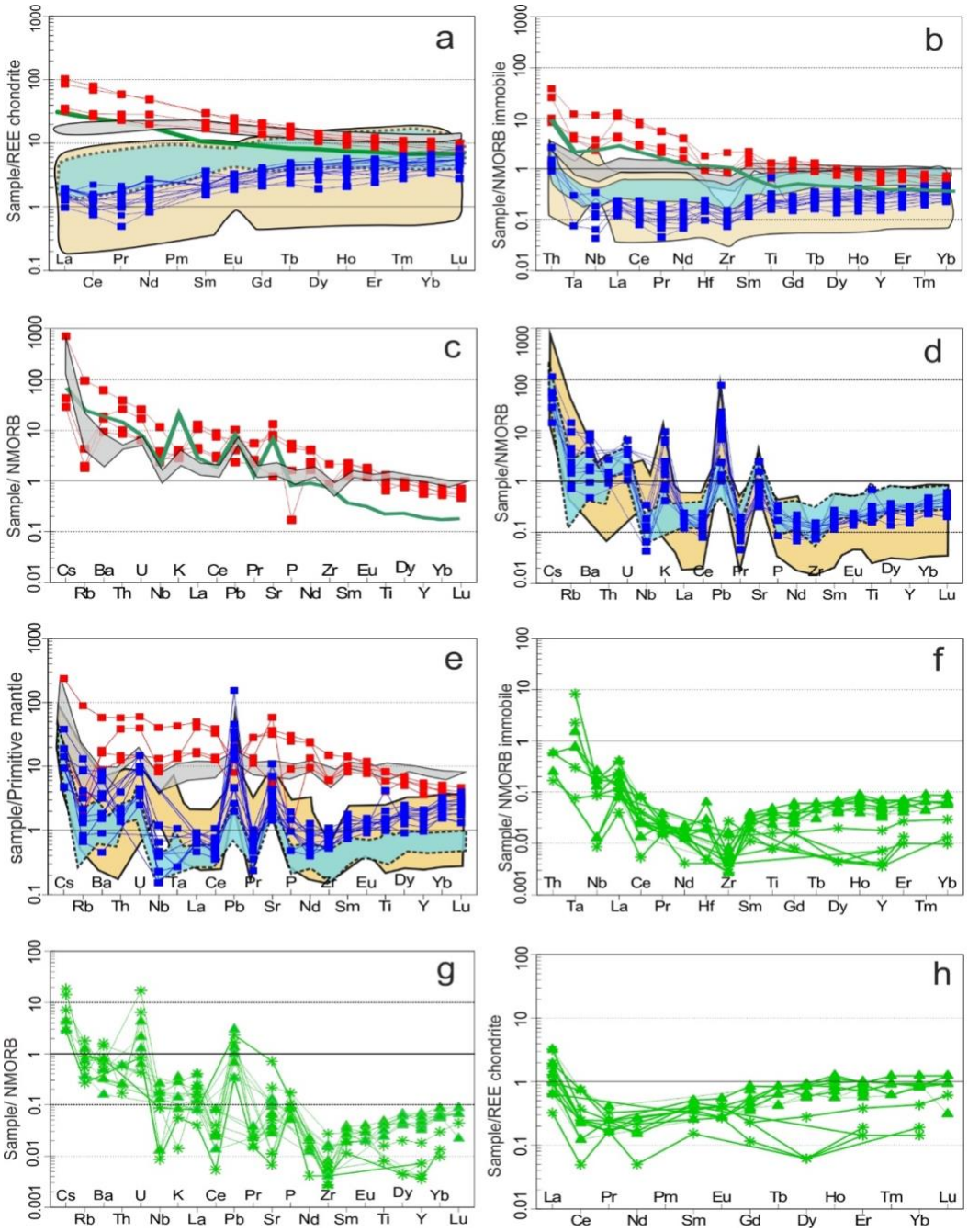

Fig. 9. Chondrite-normalized REE patterns (Boynton, 1984) for (a) gabbros and basalts, (h) pyroxenite group and dunite and serpentinite group. Multi-elements diagrams of immobile elements of (Sun and McDonough, 1989 in Pearce, 2014) for (b) gabbros and basalts, (f) pyroxenite, dunite and serpentinite samples. N-MORB-normalized diagrams for (c) gabbros, the green colour line for basaltic sample (Azizi et al., 2013) and (d) basalts. Multi-elements diagrams of Primitive Mantle for (e) gabbros and basalts and (g) pyroxenite, dunite and serpentinite samples. The light brown shaded field for the mafic rocks from the central Mawat ophiolite (Azizi et al., 2013).The grey shaded field for the mafic rocks from the southern Mawat ophiolite (Koyi et al., 2010) and the light blue shaded field for the gabbros from the western Mawat ophiolite (Mirza and Ismail, 2007). Symbols and colours as in Fig. 6.

Table 2. The whole rock geochemistry for the gabbroic rocks from the Mawat ophiolite.

Samples	9P	10a	10b	19P
N-Cood	35° 52. 24'	35° 52. 24'	35° 52. 24'	35° 50. 41'
E-Cood	45° 33. 11'	45° 33. 11'	45° 33. 11'	45° 33. 12'
Locality	Rashakani	Rashakani	Rashakani	Shakarout
Rock type	Gabbro	Gabbro	Gabbro	Gabbro
SiO2	44.44	44.08	50.83	46.11
Al2O3	11.66	18.4	18.44	15.2
Fe2O3	11.25	11.56	9.87	11.03
MgO	14.52	7.7	3.71	8.59
CaO	11.97	10.18	8.08	9.28
Na2O	2.17	3.98	5.87	4.41
K2O	0.22	0.29	0.2	0.25
TiO2	1.18	1.67	0.82	1.64
P2O5	0.19	0.02	0.63	0.51
MnO	0.17	0.13	0.12	0.17
Cr2O3	0.165	<0.002	0.002	0.047
Sc	41	27	9	24
LOI	1.7	1.6	1.2	2.4
Sum	99.66	99.64	99.77	99.61
Ba	58	107	117	386
Be	1	3	<1	2
Co	62.4	45.7	23.2	44.4
Cs	<0.1	0.3	0.2	5
Ga	13.8	16	17.8	17.7
Hf	1.9	2.2	2	3.7
Nb	8.9	5.4	6.3	26.7
Rb	1	2.4	1.1	53.1
Sn	1	1	<1	2
Sr	109.8	1181.7	734.5	632.7
Ta	0.6	0.5	0.5	1.6
Th	1	1.2	3.1	4.6
U	0.3	0.3	0.8	1.2
V	248	279	114	224
W	<0.5	<0.5	<0.5	<0.5
Zr	64.2	64.3	63.6	158.2
Y	15.6	19.8	21.9	23.9
La	10.2	11.1	26.6	32.1
Ce	21.1	23.5	55.9	65
Pr	2.82	3.5	7.18	7.32
Nd	12	17.2	30.3	29.1
Sm	3.33	4.2	5.87	5.74
Eu	1.19	1.43	1.67	1.86
Gd	3.59	4.73	5.38	5.47
Tb	0.6	0.75	0.75	0.88
Dy	3.41	4.19	4.03	4.64
Ho	0.67	0.76	0.85	0.93
Er	1.85	2.18	2.29	2.59
Tm	0.23	0.31	0.29	0.36
Yb	1.61	1.91	1.75	2.26
Lu	0.21	0.27	0.25	0.32
TOT/C	0.04	0.03	<0.02	0.02
TOT/S	<0.02	<0.02	<0.02	0.04
Mo	0.8	0.6	1.1	3.9
Cu	14.6	13.1	127.3	178.2
Pb	0.7	3.1	1.9	1.2
Zn	19	18	25	24
Ni	132.1	87	49.9	53.6
Cr	1128.93	1	13.684	321.574
As	<0.5	<0.5	<0.5	<0.5
Cd	<0.1	<0.1	<0.1	<0.1
Sb	<0.1	<0.1	<0.1	<0.1
Bi	<0.1	<0.1	<0.1	<0.1
Ag	<0.1	<0.1	<0.1	<0.1
Au	<0.5	<0.5	0.8	9.4
Hg	<0.01	<0.01	<0.01	<0.01
Tl	<0.1	<0.1	<0.1	<0.1
Se	<0.5	<0.5	<0.5	<0.5
Mg#	71.8	56.8	42.6	60.6
LaN/YbN	4.31	3.96	10.34	9.67
LaN/SmN	1.92	1.66	2.84	3.5
CeN/YbN	3.45	3.24	8.41	7.57
CeN/SmN	1.54	1.36	2.31	2.74
REE SUM	62.81	76.03	143.11	158.57
ThN	8.33	10	25.83	38.33
NbN	3.82	2.32	2.7	11.46

The ultramafic samples are rich in Cr (2278-10537 ppm), low in Sr (< 64 ppm) and the incompatible HFSE-elements Zr (< 2 ppm), Y (< 1.9 ppm), Th (< 0.2 ppm), Nb (< 0.6 ppm), Ta (< 1.1 ppm) and Ce < (0.6 ppm). The dunites and serpentinites are rich in Ni (1629 - 2864 ppm), Co (81.3 -

135.5 ppm) and low in Sc (3-24 ppm) and V (16-99 ppm). In the pyroxenite dykes, the Ni content is (186 - 974 ppm), Co is (32.9 – 110.9 ppm), Sc is (30-52 ppm), and V is (114 - 178 ppm) (Table 3).

The chondrite-normalized ultramafic samples show spoon-shaped REE patterns (Fig 9h). The ΣREE values are extremely low (0.1-2.47 ppm). The LREEs of the pyroxenites are slightly enriched relative to HREEs (La_N/Yb_N = 0.68-3.58). The dunites and serpentinites are LREE-enriched compared to HREEs (La_N/Yb_N = 1.2-16.33). The MORB-normalized immobile multi-element diagram shows humps in La and Hf and troughs in Nb, Ce and Zr and are poorer in all elements relative to N-MORB (Fig. 9f). The primitive-mantle normalized trace element diagram shows a depletion in LILEs except Cs, Pb and HFSEs which display depletion in all elements except U (Fig. 9g). The pyroxenite dykes are depleted in the LILEs and the HFSEs Th, Nb, Zr and Ti. The dunites/serpentinites show extreme depletion in the LILEs and HFSEs compared to the pyroxenites.

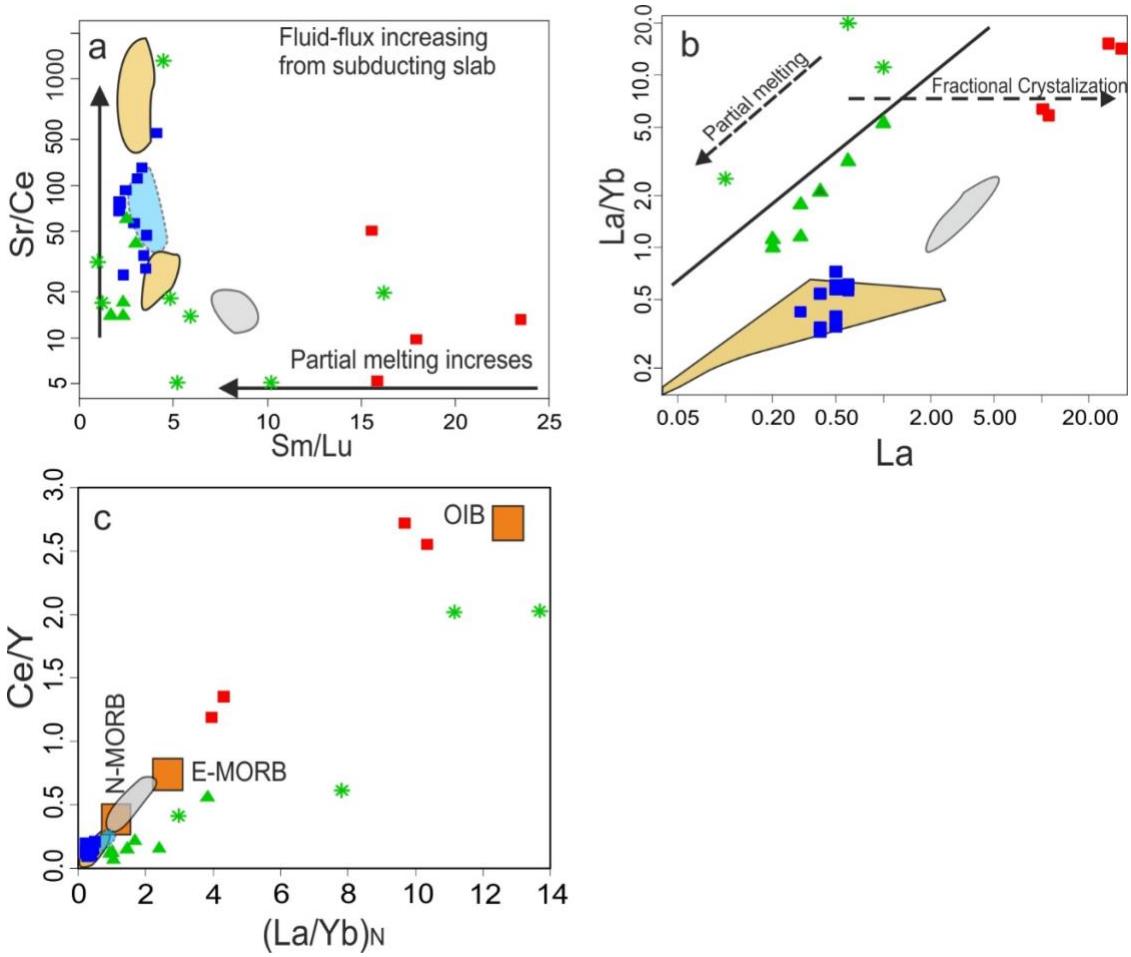

Fig. 10. (a) The partial melting and fluid flux from subducting slab ratio in mafic rocks Sm/Lu vs. Sr/Ce diagram, (b) La/Yb vs. La partial melting diagram of the studied mafic samples (Pinto-Linares et al., 2008) and (c) Ce/Y vs. La_N/Yb_N diagram (Saunders et al., 1988). Symbols and colours as in Fig. 6.

Table 3. The whole rock geochemistry for the ultramafic (dunite and serpentinite group and pyroxenite group) from the Mawat ophiolite

Samples	1D	2SD	3D	4P	6CP	20PD	21SGD
N-Cood	35° 50.52'	35° 50.52'	35° 50.52'	35° 50.52'	35° 50.46'	35° 50.44'	35° 51.28'
E-Cood	45° 31.56'	45° 31.57'	45° 31.56'	45° 31.39'	45° 33.30'	45° 31.33'	45° 32.11'
Locality	Kurdawi	Kurdawi	Kurdawi	Kurdawi	Kurdawi	Shakeh Root	Shakeh Root
Rock type	Serpentinized Dunite	Pyroxenite Dyke	Dunite	Pyroxenite Dyke	Pyroxenite Dyke	Pyroxenite Dyke	Serpentinite
SiO2	42.95	54.47	43.18	53.21	55.14	50.13	41.42
Al2O3	0.2	1.97	0.31	1.39	1.49	1.47	4.35
Fe2O3	8.61	4.65	7.59	4.41	3.55	5.01	6.23
MgO	39.14	23.8	42.15	20.24	22.4	25.1	32.74
CaO	2.14	9.76	0.61	17.01	13.07	11.97	0.24
Na2O	0.01	0.15	0.07	0.1	0.13	0.16	<0.01
K2O	<0.01	0.02	<0.001	0.01	<0.01	<0.01	<0.01
TiO2	<0.01	0.06	<0.01	0.05	0.05	0.03	0.02
P2O5	<0.01	<0.01	0.012	0.01	<0.01	<0.01	<0.01
MnO	0.12	0.11	0.11	0.09	0.06	0.1	0.12
Cr2O3	0.389	0.426	1.122	0.461	0.54	0.524	0.348
Sc	5	41	3	51	42	31	24
LOI	5.5	4.1	3.9	2.6	3.1	4.9	13.7
Sum	99.33	99.55	99.29	99.62	99.6	99.55	99.43
Ba	5	5	3	3	3	2	4
Be	<1	4	1	1	<1	<1	<1
Co	115	46.5	94.3	38.7	32.9	57.7	81.3
Cs	<0.1	<0.1	0.05	0.02	<0.1	<0.1	0.1
Ga	<0.5	1.6	0.7	1.2	0.9	1.1	2.1
Hf	<0.1	<0.1	0.04	0.13	<0.1	<0.1	<0.1
Nb	0.2	0.6	0.4	0.4	0.3	0.4	0.4
Rb	0.5	0.4	1	0.7	0.7	0.4	0.5
Sn	<1	<1	0.6	0.6	<1	<1	<1
Sr	64	6	4.5	3.4	2.8	10.7	5.2
Ta	0.3	0.1	0.04	0.1	0.1	0.2	1.1
Th	<0.2	<0.2	0.07	0.07	<0.2	<0.2	<0.2
U	<0.1	<0.1	0.02	0.06	0.1	<0.1	0.8
V	22	152	19	178	146	118	99
W	<0.5	<0.5	<0.5	<0.5	<0.5	<0.5	<0.5
Zr	0.3	0.6	0.2	0.4	0.5	1.1	1
Y	0.2	1.9	0.1	1.4	1	1.1	0.5
La	0.2	0.3	0.4	0.6	0.4	1	1
Ce	<0.1	0.1	0.2	0.2	0.2	0.6	0.3
Pr	<0.02	0.03	0.02	0.03	0.03	0.05	0.03
Nd	<0.3	<0.3	<0.01	0.09	<0.3	<0.3	<0.3
Sm	<0.05	0.1	0.08	0.07	0.05	<0.05	<0.05
Eu	<0.02	0.04	<0.01	0.03	0.02	<0.02	0.03
Gd	<0.05	0.22	<0.01	0.1	0.1	0.19	0.06
Tb	<0.01	0.04	<0.01	0.03	0.02	0.02	<0.01
Dy	<0.05	0.3	<0.05	0.28	0.21	0.18	0.09
Ho	<0.02	0.09	<0.01	0.06	0.04	0.06	<0.02
Er	<0.03	0.2	0.03	0.15	0.12	0.14	0.08
Tm	<0.01	0.04	<0.01	0.03	0.02	0.03	<0.01
Yb	<0.05	0.26	<0.05	0.19	0.19	0.19	0.09
Lu	<0.01	0.04	<0.01	0.03	0.03	0.01	0.02
TOT/C	0.43	0.04	0.14	0.05	0.02	0.05	0.05
TOT/S	<0.02	<0.02	<0.02	<0.02	<0.02	0.02	<0.02
Mo	0.9	0.3	0.9	1.5	0.8	0.5	0.2
Cu	1.4	256.6	3.4	78.1	70	126.1	1.5
Pb	0.7	<0.1	<0.1	0.9	0.4	<0.1	<0.1
Zn	12	13	3	2	1	5	16
Ni	2516.5	195.7	2864.6	187.5	186.6	858.6	1629
Cr	2661.538	2914.692	7676.724	3154.162	3694.68	3585.208	2381.016
As	0.8	<0.5	1	<0.2	<0.5	<0.5	0.9
Cd	<0.1	<0.1	<0.1	<0.1	<0.1	<0.1	<0.1
Sb	<0.1	<0.1	<0.1	<0.1	<0.1	<0.1	<0.1
Bi	<0.1	<0.1	0.04	<0.1	<0.1	<0.1	<0.1
Ag	<0.1	<0.1	<0.1	<0.1	<0.1	<0.1	<0.1
Au	<0.5	9.6	<0.5	2.9	1.2	6.2	<0.5
Hg	<0.01	<0.01	<0.01	<0.01	<0.01	0.02	<0.01
Tl	<0.1	<0.1	<0.1	<0.1	<0.1	<0.1	<0.1
Se	<0.5	<0.5	<0.5	<0.5	<0.5	<0.5	<0.5
Mg#	90	91	91.6	90	92.5	90.8	91.2
LaN/YbN	5.44	0.79	10.89	2.15	1.43	3.58	7.56
LaN/SmN	5.01	1.88	3.13	5.37	5.01	25.06	25.06
CeN/YbN	0.48	0.24	0.61	0.69	0.97	5.82	2.91
CeN/SmN	0.48	0.24	0.61	0.69	0.97	5.82	2.91
REE SUM	0.2	1.76	0.7	1.77	1.43	2.47	1.7
ThN	0.83	0.83	0.58	0.58	0.83	0.83	0.83
NbN	0.09	0.26	0.17	0.17	0.13	0.17	0.17

Samples	28SC	D1/1	D3/1	D3/3	D3/4	D3/5	D3/6	D3/7
N-Cood	35° 52.41'	35° 48. 56'	35° 49. 32'	35° 50. 38'	35° 50. 52'	35° 50. 52'	35° 51. 26'	35° 51. 26'
E-Cood	45° 32.57'	45° 29. 09'	45° 34. 20'	45° 33. 09'	45° 33. 03'	45° 33. 03'	45° 33. 36'	45° 33. 36'
Locality	Rashakani	Kwnjrin	Shakeh Root	Ser Shiw	Ser Shiw	Ser Shiw	Ser Shiw	Top of Ser Shiw
Rock type	Serpentinite	Serpentinite	Dunite	Pyroxenite	Dunite	Dunite	Pyroxenite	Pyroxenite
SiO2	42.2	39.78	41.25	53.27	40.22	41.35	55.11	53.67
Al2O3	0.37	0.69	0.47	1.32	0.85	0.15	1.15	0.97
Fe2O3	8.19	8.39	8.57	3.71	10.49	9.14	3.09	4.17
MgO	33.82	35.41	41.57	21.91	44.1	47.41	24.89	27.56
CaO	0.26	0.1	0.47	17.12	0.67	0.19	11.69	10.44
Na2O	0.06	0.01	0.02	0.1	<0.01	0.07	0.13	0.11
K2O	0.001	<0.001	<0.01	0.025	<0.01	0.004	<0.01	<0.01
TiO2	0.01	<0.01	<0.01	0.05	0.01	<0.01	0.04	0.03
P2O5	0.02	0.01	0.01	0.01	0.02	0.01	<0.01	<0.01
MnO	0.1	0.11	0.12	0.08	0.14	0.12	0.05	0.07
Cr2O3	0.387	0.445	0.388	0.43	1.54	0.402	0.4	0.333
Sc	6	11	10	50	9	6	52	39
LOI	13.8	14.7	6.8	1.7	1.6	0.8	3.2	2.4
Sum	99.42	99.93	99.94	99.85	99.91	99.94	99.91	99.91
Ba	10	9	<1	<0.5	<1	<0.5	<1	1
Be	2	<1	<1	<0.2	<1	<0.2	<1	<1
Co	108.9	106.5	111.2	40.8	135.2	128.9	41.8	55.9
Cs	0.13	0.03	<0.1	<0.01	<0.1	0.02	<0.1	<0.1
Ga	0.7	0.9	<0.5	0.7	0.7	0.5	<0.5	<0.5
Hf	0.01	0.01	<0.1	0.04	<0.1	<0.01	<0.1	<0.1
Nb	0.2	0.2	<0.1	0.03	<0.1	0.02	<0.1	<0.1
Rb	0.3	0.2	0.2	0.2	0.5	0.15	0.2	0.2
Sn	0.6	0.8	<1	0.6	<1	0.4	<1	<1
Sr	19.5	3	1	8.3	1	0.6	11.5	9.2
Ta	0.01	<0.01	<0.1	<0.01	<0.1	<0.01	<0.1	<0.1
Th	0.02	<0.01	<0.2	0.03	<0.2	<0.01	<0.2	<0.2
U	0.3	0.04	<0.1	0.03	<0.1	0.04	<0.1	<0.1
V	23	43	39	172	83	16	167	124
W	<0.5	<0.5	<0.5	<0.5	<0.5	0.5	<0.5	<0.5
Zr	2	0.2	0.2	0.4	0.4	0.3	1.2	0.3
Y	0.2	0.12	<0.1	1.9	0.1	0.1	1.6	0.9
La	0.6	0.3	0.2	0.2	0.5	0.1	0.2	0.2
Ce	0.6	0.6	<0.1	0.2	0.2	0.04	<0.1	0.1
Pr	0.04	0.03	<0.02	<0.01	<0.02	0.02	<0.02	<0.02
Nd	<0.3	0.13	<0.3	0.1	<0.3	0.03	<0.3	<0.3
Sm	<0.01	0.05	<0.05	0.09	<0.05	0.03	<0.05	<0.05
Eu	0.03	0.02	<0.02	0.03	<0.02	<0.01	0.02	<0.02
Gd	0.06	0.03	<0.05	0.14	<0.05	<0.01	0.12	0.09
Tb	<0.01	<0.01	<0.01	0.03	<0.01	<0.01	0.04	0.03
Dy	0.02	0.02	<0.05	0.27	<0.05	0.02	0.28	0.21
Ho	<0.01	<0.01	<0.02	0.07	<0.02	<0.01	0.08	0.04
Er	0.03	0.04	<0.03	0.21	<0.03	<0.01	0.21	0.17
Tm	<0.01	<0.01	<0.01	0.03	<0.01	<0.01	0.03	0.02
Yb	0.03	<0.01	<0.05	0.2	<0.05	0.04	0.18	0.18
Lu	<0.01	<0.01	<0.01	0.03	<0.01	<0.01	0.04	0.03
TOT/C	0.06	0.05	0.07	0.07	0.06	0.04	0.03	0.03
TOT/S	<0.02	0.03	<0.02	<0.02	<0.02	<0.02	<0.02	0.04
Mo	0.2	0.4	0.4	0.6	1	0.7	0.3	0.6
Cu	8.3	13.4	4.8	633.9	5.3	5.4	112.7	145.4
Pb	<0.1	0.3	0.3	0.2	0.5	0.1	0.1	0.3
Zn	18	17	21	3	22	25	2	6
Ni	2097	2277.2	2416.7	295.7	2402.6	2664.2	215.8	974.4
Cr	2647.854	3044.69	2654.696	2942.06	10536.68	2750.484	2736.8	2278.386
As	1.1	2.9	0.6	<0.5	0.8	0.5	0.5	1.6
Cd	<0.1	<0.1	<0.1	<0.1	<0.1	<0.1	<0.1	<0.1
Sb	<0.1	<0.1	<0.1	0.2	<0.1	1.1	<0.1	<0.1
Bi	0.08	0.08	<0.1	0.5	<0.1	<0.02	<0.1	<0.1
Ag	<0.1	<0.1	<0.1	0.4	<0.1	<0.1	<0.1	<0.1
Au	<0.5	1.2	0.8	195.2	2.4	2.9	14.3	32.5
Hg	<0.01	<0.01	<0.01	0.07	<0.01	<0.01	<0.01	<0.01
Tl	<0.1	<0.1	<0.1	<0.1	<0.1	<0.1	<0.1	<0.1
Se	<0.5	<0.5	<0.5	<0.5	<0.5	<0.5	<0.5	0.9
Mg#	89.1	89.3	90.5	92.1	89.2	91.1	94.1	92.9
LaN/YbN	16.33	8.17	5.44	0.68	13.61	2.72	0.76	0.76
LaN/SmN	15.04	7.52	5.01	5.01	12.53	2.51	5.01	5.01
CeN/YbN	5.82	5.82	0.48	1.94	1.94	0.48	0.48	0.97
CeN/SmN	5.82	5.82	0.48	1.94	1.94	0.48	0.48	0.97
REE SUM	1.24	0.97	0.2	1.41	0.7	0.1	1.2	1.07
ThN	0.04	0.83	0.25	0.83	0.04	0.83	0.83	0.83
NbN	0.09	0.02	0.01	0.02	0.01	0.02	0.02	0.02

5. Discussion

5.1. Petrogenesis

The mafic and ultramafic rocks are affected by various degrees of alteration, which resulted in partial to complete replacement of many of the essential rock-forming minerals and increased the loss on ignition (LOI). Three serpentinites have the highest LOI ranging between 13 and 14 wt. %, whereas, the highest LOI in the mafic rocks is < 5.9 wt. %. During such alterations, many of the major elements such as SiO_2, K_2O, Na_2O and MgO, as well as LILEs and LREEs, generally show variable degree of mobilization. In contrast, the HFSEs (e. g., Ti, Zr, Y, Nb, Ta, Hf and Th), MREEs and HREEs as immobile elements, are useful for petrogenetic and tectonic studies (Karakaya, 2009).

5.1.1. Basalts and gabbros

The mafic samples show compositional variations, which could be related to mantle heterogeneity. (Pearce and Norry, 1979; Pearce, 1983). The differences in the REE-patterns and the key element ratios (e.g. La/Yb_N, Zr/Y, Nb/Y) between the basalts and gabbros cannot be explained by various degree of partial melting alone. Instead, differences in the magma sources are more likely. The basaltic rocks are slightly enriched in the HREEs relative to LREEs *[$(La/Yb)_N$ =0.22-0.49]* with positive Ba, U, K, Pb and Sr anomalies and negative Nb, Zr, and Ti in the N-MORB normalized diagram (Fig. 9d) suggesting that the basalts formed by partial melting of a depleted mantle. These features resemble those of the boninites formed in a forearc setting related to initial intra-oceanic subduction settings (Shervais et al., 2019). The subduction additions and degree of fluid flux from the subducting slab to the mantle wedge can be deduced from the ratios of highly fluid-mobile to less fluid-mobile or fluid-immobile elements (e.g. Sr/Ce) (Wehrmann et al., 2014). Based on the Sm/Lu vs. Sr/Ce diagram, the basaltic rocks show higher degree of partial melting relative to the gabbros (Fig. 10a) and the La/Yb vs. La diagram (Pinto-Linares et al., 2008) confirms the results of Fig. 10a, showing that both the gabbros and basalts follow the partial melting trend and the basalts have higher degree of partial melting (Fig. 10b). High Ce/Y and La_N/Yb_N ratios in mafic rocks are an indication for low degree of partial melting process or that the mafic rocks were derived from enriched sources (Saccani et al., 2003; Fig. 10c). Therefore, the values of Ce/Yb (0.08-0.2) and La_N/Yb_N (0.22-0.49) in the basaltic samples are lower than those in the gabbroic samples (1.18-2.7 and, 3.9-10.3 respectively). This suggests that the basalts formed by higher degree of partial melting of a depleted-mantle source compared to the gabbros. The basaltic samples show low Nb (0.1-0.79 ppm) and Zr (5.7-11.5 ppm) contents relative to N-MORB (Nb = 2.33 ppm and Zr =74 ppm, respectively) indicating that the basaltic rocks were formed from a depleted mantle source. In contrast, the gabbroic samples show high Nb 5.4-26.7 ppm, and Zr 63.6-158.2 ppm implying that these rocks were derived from an enriched mantle source (Sun and McDonough, 1989). The mafic rocks from the central MO show variable low consentrations of Nb (0.9 – 6.0 ppm) and low Zr (1.3 – 6.7 ppm) except for one sample which has Zr content of 66.0 ppm. The gabbros from the western MO are low in Nb (0.24-0.71 ppm) and Zr (7-28 ppm).

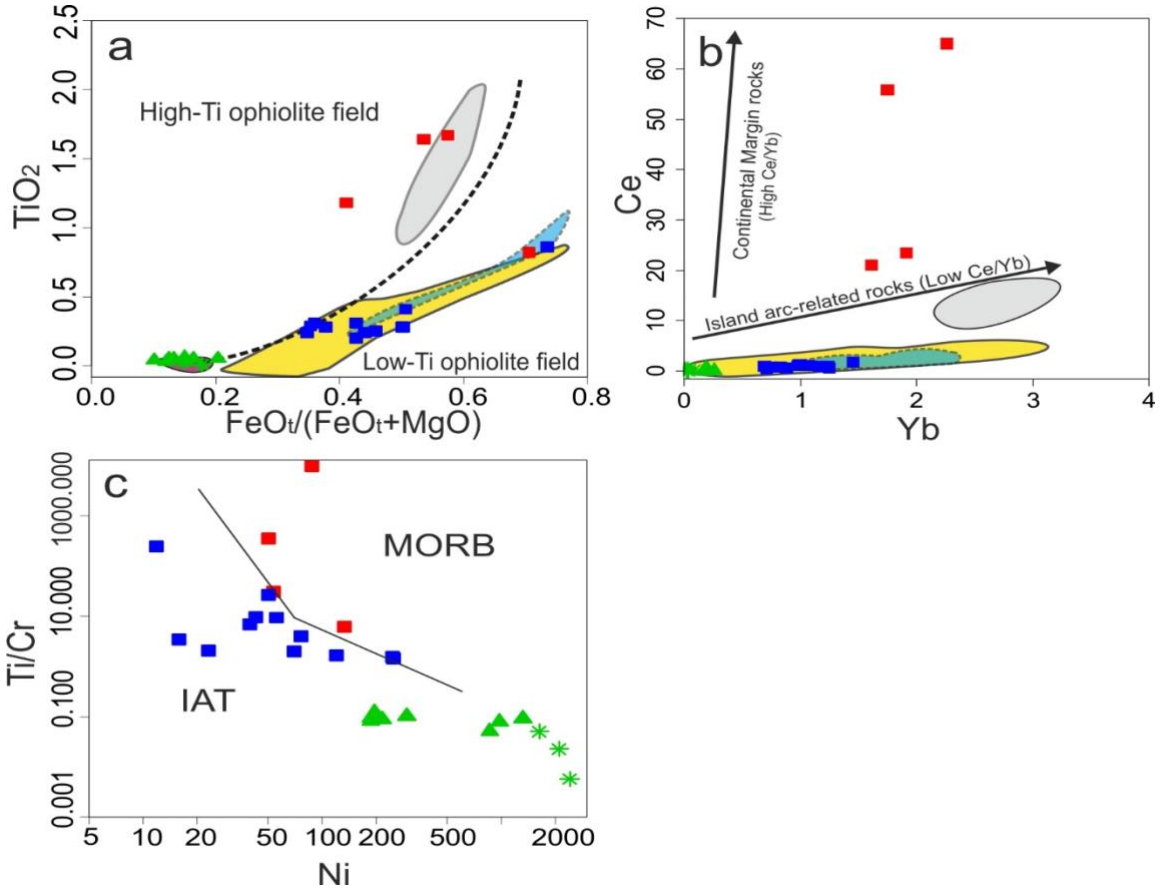

Fig. 11. (a) TiO_2 vs. $FeO^t/(FeO^t + MgO)$ diagram (Serri, 1981), (b) Ce vs Yb diagram (Hawkesworth et al., 1993), (c) Ni vs Ti/Cr diagram shows indication of island arc region for the mafic and ultramafic rocks (Beccaluva et al., 1983). Symbols and colours as in Fig. 6.

Ophiolites have been grouped into high-Ti, low-Ti and very low-Ti types. The high-Ti ophiolites display characteristics of the MORB-like magmas, occurring at mid-ocean ridges and well developed marginal basins. The low-Ti, and very low-Ti ophiolites are comparable to IAT and boninite-like magmas, respectively, formed in an intra-oceanic island arc setting (Beccaluva et al., 1989; Fig. 11a). Partial melting and re-melting of the mantle peridotite can lead to Ti-poor magmas (Hébert and Laurent, 1990). Low-Ti magma is a source for the basaltic and plutonic rocks formed in a suprasubduction zone setting (Camuzcuoğlu et al., 2017). The compositions in the Mawat data show that the basaltic rocks are low in Ti and classifies to the low-Ti ophiolites. Accordingly, the basaltic rocks derived from a low-Ti magma. The gabbroic rocks show high-Ti contents characteristic for MORB-like magmas (Fig. 11a).

5.1.2. Ultramafic rocks

The REE patterns of the ultramafic samples are slightly enriched in LREEs compared to MREEs and HREEs, showing a spoon-shaped pattern with extremely low ΣREEs. Both the dunite/serpentinite and the pyroxenite groups plot below the N-MORB reference line (Fig. 9h). The N-MORB and primitive mantle-normalized multi-element diagrams show two pattern types. The first type is the dunites and serpentinites which are extremely depleted in LIL and some HFS elements. The second type is the pyroxenite group which is less depleted in LIL and some HFS elements compared to the dunite/serpentinite group. The ultramafic samples show positive U, Pb and La anomalies and negative Nb, Ta and Zr anomalies. These features suggest that their parental magmas are derived from highly depleted mantle (Fig. 9g).

The low Ce/Yb ratios in the ultramafic samples show an island arc-related trend (Fig. 11b). The Ni vs. Ti/Cr diagram also indicates an island arc setting. (Fig. 11c). The Ti/V diagram suggests a boninite-like magma (Fig. 12b). The pyroxenite dykes are characterized by high MgO and SiO_2 (Table 3) and the low Nb/Yb ratios are consistent with their derivation from a highly depleted mantle source.

- *Tectonic Setting*

Ophiolites can form in various subduction-unrelated and subduction-related tectonic settings (e.g., Furnes et al., 2020). The tectonic setting of the MO has been controversial. An earlier work on the mafic rocks from the western MO indicated a MORB and volcanic arc basaltic affinities and tectonic settings (Mirza and Ismail, 2007). Ismail et al. (2010) suggested the suprasubduction zone affinity which is supported by the chemical composition of the chromitites and presence of associated boninites in the MO. A more recent work on the mafic and ultramafic rocks by Azizi et al. (2013) concluded that the isotope ratios, REE patterns and major and trace element contents are not consistent with the MORB, island arc or suprasubduction zone settings. Instead, the geochemical data suggest a mantle plume setting. Geochemical compositions, especially trace elements, are effective tools to infer the tectonic settings of ophiolites. Several proxies have been developed to geochemically separate different ophiolite types and their tectonic settings (e.g., Pearce, 2014, Furnes et al., 2020). In this study, we use the Nb/Y vs Zr/Ti diagram (Pearce, 1996) for classification purposes, Zr/Y vs Th/Yb diagram to distinguish tholeitic from calc-alkaline basalts (Furnes et al., 2020), Nb/Yb vs Th/Yb diagram (Pearce, 2008) to separate the subduction-unrelated ophiolites from the subduction-related ophiolites, as well as the Ti/V diagram (Shervais, 1982) to identify the forearc basalts. These are based on immobile elements to minimise the effect of alteration.

Tectonic setting can be determined by using discrimination diagram of Th/Yb vs. Nb/Yb (Pearce, 2008). It shows that the mafic rocks fall above the MORB-OIB array. The basaltic rocks fall in the oceanic arc field and the gabbros in the continental arc field. The data above the MORB-OIB array is explained by variable enrichment of elements transported by hydrous fluids with or without melts released from subducted oceanic slab. This suggests a subduction-related type setting (Furnes et al., 2020; Fig. 12a). The subduction-related type includes backarc, backarc to forearc, forearc, and volcanic arc settings. Their compositions plot in the oceanic arc and overlap the oceanic arc/continental arc fields in the Th/Yb vs Nb/Yb diagram (Pearce, 2008). Moreover, the backarc type is characterized by the MORB basalts and the backarc to forearc and forearc types are characterized by IAT and boninite type magmas.

The Ti/1000 vs. V diagram discriminates the magmas of boninite, island-arc (IAT), MORB and alkali basalts. The ultramafic and basaltic samples plot in the boninite field, where the Ti/V ratio is <10. The gabbroic samples plot in the MORB field. The mafic rocks from the western and central parts from the MO (Mirza and Ismail, 2007; Azizi et al., 2013) plot in the boninite-IAT fields with Ti/V is <10-20, while the samples in Koyi et al. (2010) from the southern MO plot in the MORB field (Fig. 12 b).

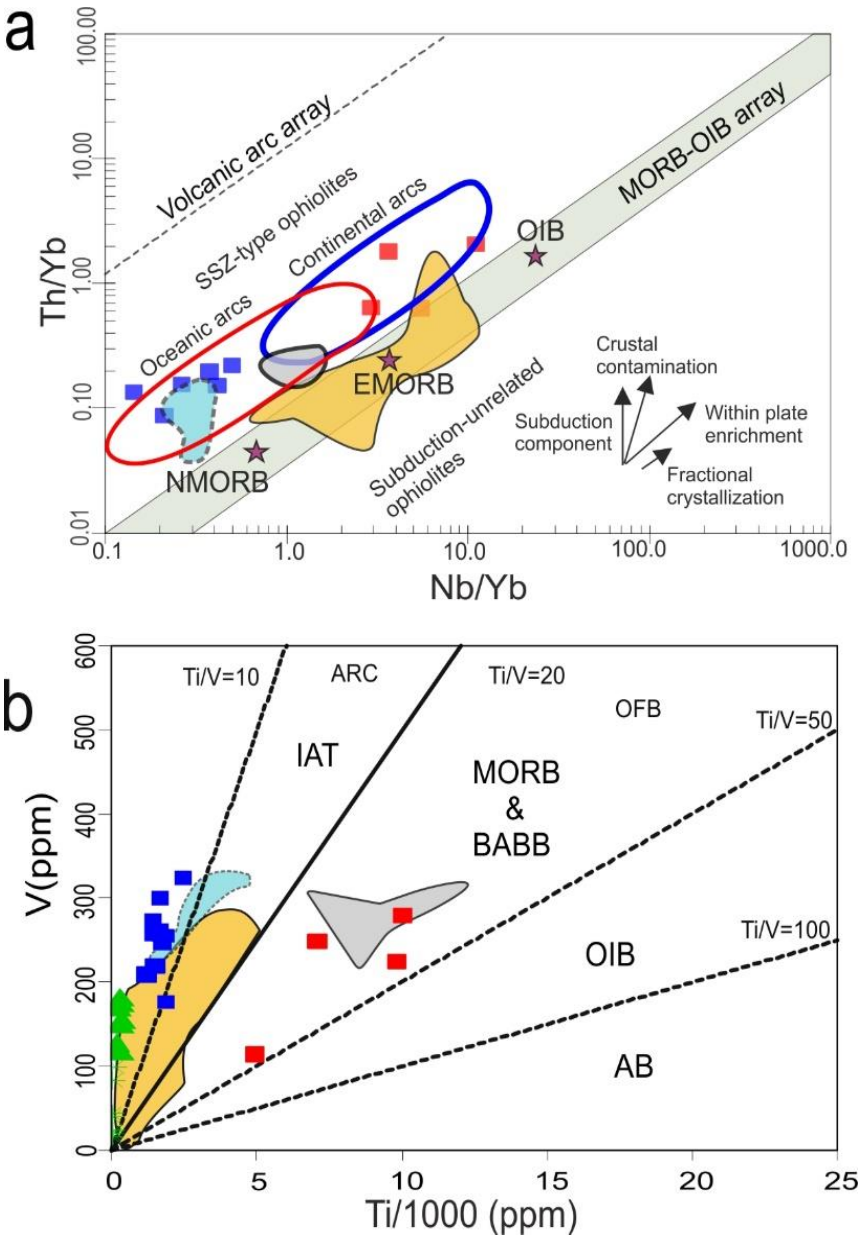

Fig. 12. (a) Th/Yb vs. Nb/Yb diagram of (Pearce, 2014), (b) Ti/1000 vs. V diagram of (Shervais, 1982). Symbols and colours as in Fig. 6.

The suprasubduction zone ophiolites often contain geochemical stratigraphy of island arc tholeiites IAT, boninite affinity and lavas of MORB compositions (Pearce, 2003). The mafic rocks of MO have boninite, IAT and MORB-like compositions. Therefore, these rocks (MORB, IAT and boninites) were formed within the same forearc region, probably with early MORB-like (Reagan et al., 2010) and younger boninitic lavas, as is common in forearc settings (Ishizuka et al., 2014). In Mawat the stratigraphic order is disrupted by thrusting (Fig. 13) and now the ultramafic (harzburgite and dunite) rocks are on the top, the amphibole gabbros are in the middle and the basalts are at the bottom. The MORB- like rocks (Koyi et al., 2010; Azizi et al., 2013) are located in the southern and central part of the MO on top of the younger sedimentary rocks (Red Beds). The boninitic rock are located in the northern MO. This indicate that, in spite of thrusting, the MO has at large preserved some of its internal stratigraphy with MORB-like rocks at botttom and boninites on top (cf. Furnes et al., 2020).

The basaltic and gabbroic rocks were derived from different sources. The gabbros were dated at ~ 80 Ma, while the felsic dykes crosscutting the mafic rocks are ~ 95 Ma (Al Humadi et al., 2019). The gabbros are interpreted as rift-related in an extensional setting above the subduction zone setting after the ophiolite formation (Al Humadi et al., 2018). The gabbros of the similar age are found in the Kermanshah ophiolite (Ao et al., 2016). Recent studies on the Tethyan ophiolites show that most ophiolites have subduction zone chemical characteristics of the suprasubduction zone ophiolite type. (Dilek, et al., 2007). The ultramafic and mafic rocks of the MO show subduction influence in terms of the trace-element contents and is very similar to other ophiolites formed by initial subduction in a forearc of suprasubduction zone environment. That is similar to the late Jurassic-Cretaceous ophiolites in the Tauride-Pontide (Turkey), Zagros (Iran) and Himalayan ophiolites to the east showing geochemical characteristics of suprasubduction zone environment (Malpas et al., 2003).

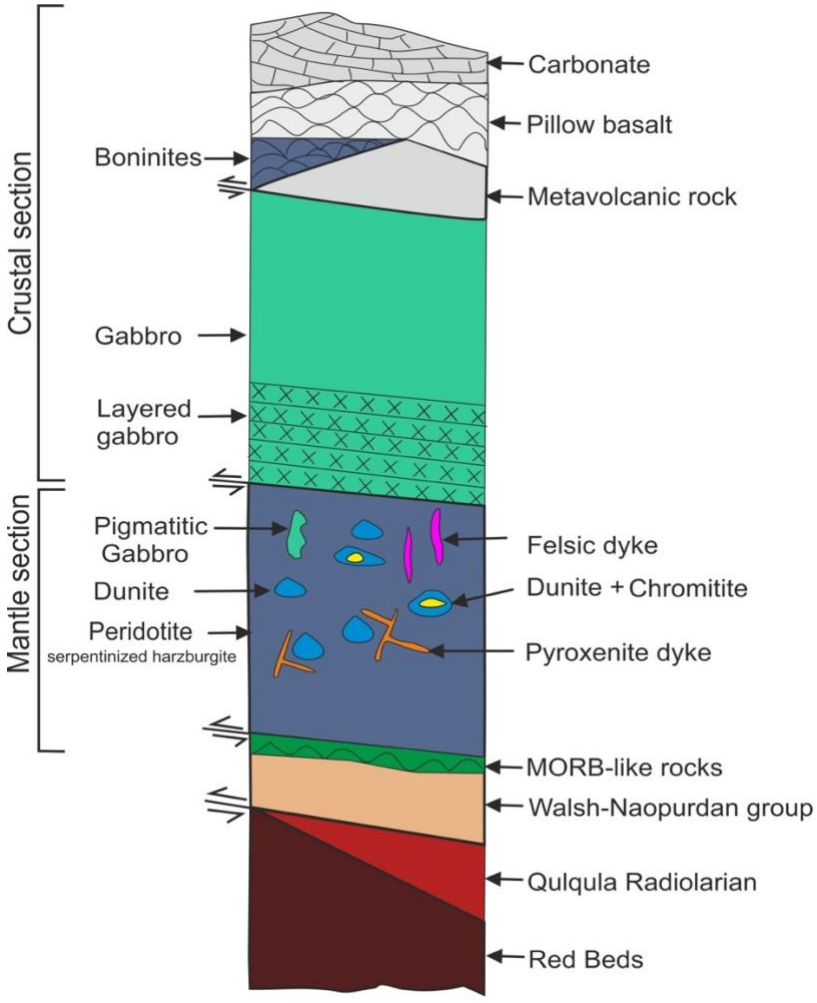

Fig. 13. Simplified section of the Mawat ophiolite showing the main rock types and the locations of the boninites and MORBs.

6. Conclusions

The major and trace element analyses of the mafic and ultramafic rocks from the Mawat ophiolite lead to the following conclusions:

- Three rock types occur in the mantle section: the dunites, serpentinites and later pyroxenites dykes. They were derived from an extremely depleted mantle.
- Three geochemical types of mafic rocks occur in the crustal section: boninites, IAT and MORB. The ≥ 15 Ma younger gabbros are enriched compared to the other mafic rocks.
- The geochemical data indicate that MORB-like rocks occur at the bottom and the boninites on the top of the ophiolite. This stratigraphy is typical for suprasubduction zone ophiolites.
- The mafic rocks were formed in a forearc region and the geochemical data are consistent with the suprasubduction zone tectonic setting. The geochemical characteristics show that Mawat is one of the suprasubduction zone ophiolites in the eastern Mediterranean region.

Acknowledgements

The authors are very gratful to Arto Peltola for making the majority of the polished thin sections.

References

Agard, P., Omrani, J., Jolivet, L., Whitechurch, H., Vrielynck, B., Spakman, W., Monié, P., Meyer, B.and Wortel, R., 2011. Zagros orogeny: a subduction-dominated process. Geological Magazine, 148, 692-725.

Alavi, M., 2007. Structures of the Zagros Fold-Thrust Belt in Iran. American Journal of Science 308, 104-104.

Al Humadi, H., Ismail, S.A. and Väisänen, M., 2018. Evidence of rifting over the suprasubduction zone Mawat Ophiolite NE, Iraq: implication for late-stage gabbro formation. In: 8th Geochemistry Symposium, Antalya 2-6 May 2018. Karadeniz Technical University of Turkey, Abstract Book,. 96.

Al Humadi, H., Väisänen, M., Ismail, S.A., Kara, J., O' Brien, H., Lahaye, Y. and Lehtonen, M., 2019. U–Pb geochronology and Hf isotope data from the Late Cretaceous Mawat ophiolite, NE Iraq. Heliyon, 5.

Al Humadi, H.S., Väisänen, M., Ismail, S.A., Lehtonen, M. and Johanson, B., 2021. Subducted basalts and sediments as sources for felsic dykes in the Mawat ophiolite, NE Iraq. Ofioliti, 46, 27–41.

Ali, S.A., Buckman,, S., Aswad, K. J., Jones, B.G., Ismail, S.A. and Nutman, A.P., 2013. The tectonic evolution of a Neo-Tethyan (Eocene–Oligocene) island-arc (Walash and Naopurdan groups) in the Kurdistan region of the Northeast Iraqi Zagros Suture Zone. Island Arc, 22, 104–125.

Ali, S.A., Nutman A.P., Aswad K.J. and Jones B.G., 2019. Overview of the tectonic evolution of the Iraqi Zagros thrust zone: Sixty million years of Neotethyan ocean subduction. Journal Geodynamics, 129, 162-177.

Allahyari, K., Saccani, E., Rahimzadeh, B. and Zeda, O., 2014. Mineral chemistry and petrology of highly magnesian ultramafic cumulates from the Sarve-Abad (Sawlava) ophiolites (Kurdistan, NW Iran): New evidence for boninitic magmatism in intra-oceanic fore-arc setting in the Neo-Tethys between Arabia and Iran. Journal of Asian Earth Sciences, 79, 312-328.

Al-Kadhimi, J.A.M., Sissakian, V.K., Fattah, A.S., Deikran, D.B., 1996. Tectonic Map of Iraq. Geological Survey and Mining of Iraq, 38.

Al-Qayim B., Omer A. and Koyi H., 2012. Tectonostratigraphic overview of the Zagros suture zone, Kurdistan region, Northeast Iraq. GeoArabia, 17, 109-156.

Anonymous, 1972. Penrose field conference on ophiolites. Geotimes, 17, 24-25.

Ao, S., Xiao, W., Jafari, M. K., Talebian, M., Chen, L., Wan, B., Ji, W..and Zhang, Z., 2016. U–Pb zircon ages, field geology and geochemistry of the Kermanshah ophiolite (Iran): From continental rifting at 79 Ma to oceanic core complex at ca. 36 Ma in the southern Neo-Tethys. Gondwana Research, 31, 305-318.

Ao, S., Mao, Q., Khalatbari-Jafari, M., Windley, B.F., Song, D., Zhang, Z., Zhang, J., Wan, B., Han, C. and Xiao, W., 2021. U–Pb age, Hf–O isotopes, and geochemistry of the Sardasht ophiolite in the NW Zagros orogen: Implications for the tectonic evolution of Neo-Tethys. Geological Journal, 56, 1315-1329.

Arai, S., Shimizu, Y., Ismail, S. A. and Ahmed, A. H., 2006. Low-T formation of high-Cr spinel with apparently primary chemical characteristics within podiform chromitite from Rayat, northeastern Iraq. Mineralogical Magazine, 70, 499-508.

Aziz, N.R.H. 2008. Petrogenesis, Evolution, and Tectonics of the Serpentinites of the Zagros Suture Zone, Kurdistan Region, NE Iraq. Dissertation. University of Sulaimani, 250.

Azizi, H., Hadi A., Asahara Y.and Mohammad Y.O., 2013. Geochemistry and geodynamics of the Mawat mafic complex in the Zagros Suture zone, northeast Iraq. Central Europian Journal of Geosciences, 5, 523–537.

Beccaluva, L., Di Girolamo P., Macciotta G.and Morra V., 1983. Magma affinities and fractionation trends in ophiolites. Ofioliti, 8, 307–324.

Beccaluva, L., Macciotta G., Piccardo G.B.and Zeda O., 1989. Clinopyroxene composition of ophiolite basalts as petrogenetic indicator. Chemical Geology 77, 165-182.

Boynton W., V. 1984. Cosmochemistry of the rare earth elements: meteorite studies. In: Henderson R (ed.) Rare Earth Element Geochemistry. Developments in Geochemistry. Elsevier 2, 63-114.

Buda, G.and Al-Hashimi, W.S., 1977. Petrology of Mawat ophiolite complex, Northern Iraq. Journal of Geological Society of Iraq, 10, 69-98.

Camuzcuoğlu M., Bağcı U., Koepke J. and Wolff P., E., 2017. Tectonic significance of the cumulate gabbros within Kuluncak Ophiolitic suite (Malatya, SE Turkey) inferred from geochemical data. Ofioliti, 42, 81-103.

Dilek, Y. and Ahmed, Z., 2003. Proterozoic ophiolites of the Arabian Shield and their significance in Precambrian tectonics. Geological Society London, Special Publication, 218, 685-700.

Dilek Y. and Furnes H., 2014. Ophiolites and their origins. Elements, 10, 93–100.

Dilek Y., Furnes H. and Shallo, M., 2007. Suprasubduction zone ophiolite formation along the periphery of Mesozoic Gondwana. Gondwana Reseach, 11, 453–475.

Furnes, H., De Wit, M. and Dilek, Y., 2014. Four billion years of ophiolites reveal secular trends in oceanic crust formation. Geoscience Frontiers, 5, 571–603.

Furnes, H., Dilek, Y., Zhao, G., Safonova I.and Santosh M., 2020. Geochemical characterization of ophiolites in the Alpine-Himalayan Orogenic Belt: Magmatically and tectonically diverse evolution of the Mesozoic Neotethyan oceanic crust. Earth Sci. Rev., 103258.

Hawkesworth, C. J., Gallagher K., Hergt J. M.and McDermott F. 1993. Mantle and slab contributions in arc magmas. Ann. Rev. Earth Planet Science, 21, 75-204.

Hébert, R.and Laurent, R., 1990. Mineral chemistry of the plutonic section of the Troodos ophiolite: new constraints for genesis of arc-related ophiolites. In: Malpas J., Morres E.M., Panayiotou A.and Xenophontos C., (Eds) Ophiolites: Proceeding of the Symposium "Troodos 1987". Geological Survey Department of Nicosia, Cyprus, 149-163.

Hirano, N., Ogawa Y., Saito K., Yoshida T., Sato H.and Taniguchi H. 2003. Multi-stage evolution of the Tertiary Mineoka ophiolite, Japan: new geochemical and age constraints. Geological Society, London, Special Publication, 218, 279-298.

Ishizuka, O., Tani, K.and Reagan, M. K., 2014. Izu-Bonin-Mariana forearc crust as a modern ophiolite analogue. Elements, 10, 115–120.

Ishikawa, A., Kaneko, Y., Kadarusman, A. and Ota, T., 2007. Multiple generations of forearc mafic–ultramafic rocks in the Timor–Tanimbar ophiolite, eastern Indonesia. Gondwana Res. 11:200-217.

Ismail, S. A., Mirza, T. M. and Carr, P. F., 2010. Platinum-group elements geochemistry in podiform chromitites and associated peridotites of the MO, northeastern Iraq. Journal Asian Earth Science, 37, 31–41.

Ismail, S. A., Ali, S. A., Nutman, A. P., Bennett, V. C. and Jones, B. G., 2017. The Pushtashan juvenile suprasubduction zone assemblage of Kurdistan northeastern Iraq: A Cretaceous Cenomanian Neo-Tethys missing link. Geoscie. Front. 8:1073-1087.

Ismail S. A., Koshnaw, R. I., Barber, D. E., Al Humadi, H. and Stockli, D. F., 2020. Generation and exhumation of granitoid intrusions in the Penjween ophiolite complex, NW Zagros of the Kurdistan region of Iraq: Implications for the geodynamic evolution of the Arabian-Eurasian collision zone. Lithos, 376, 105714.

Jahn, B. M., 1986 Mid-ocean ridge or marginal basin origin of the East Taiwan Ophiolite: chemical and isotopic evidence. Contrib. Mineralogy Petrology, 92, 194–206.

Janoušek V., Farrow C.M.and Erban V., 2006. Interpretation of whole-rock geochemical data in igneous geochemistry: introducing Geochemical Data Toolkit (GCDkit). Journal Petrology, 47,1255-1259.

Jassim, S. Z., 1972. Geology of the central sector of the Mawat Igneous Complex. Manuscript report, GEOSURV, Baghdad Iraq.

Jassim ,S. Z., 1973. Geology of the central sector of Mawat complex. Journal Geological Society, Iraq, 6, 82-92.

Jassim, S. Z.and Goff, J. C., (Eds). 2006. Geology of Iraq. Dolin, Prague and Moravian Museum, Brno, 341.

Karakaya, N., 2009. REE and HFS element behaviour in the alteration facies of the Erenler Dağı Volcanics (Konya, Turkey) and kaolinite occurrence. J. Geochem. Explor. 101,185–208.

Koy,i A. M. A., Sofyissa, M. M.and Jamee,l N. M., 2010. Geochemistry of metagabbros from Southern Mawat ophiolite complex, NE Iraq. Journal of Pure Sciences 22, 4.

Le Bas M. J., 2000. IUGS reclassification of the high-Mg and picritic volcanic rocks. J. Petrol. 41:1467-1470.

Malpas, J., Zhou, M.-F., Robinson, P.T., Reynolds, P.H., 2003. Geochemical and geochronological constraints on the origin and emplacement of the Yarlung Zangbo ophiolites, Southern Tibet. In: Dilek, Y., Robinson, P.T. (Eds.), Ophiolites in Earth History. Geological Society of London Special. 218, 191–206.

Middlemost, E. A. K., 1994. Naming materials in the magma/igneous rock system. Earth Science Review, 37, 215-224.

Mirza, T. A.and Ismail, S. A., 2007. Origin of plagiogranite in the Mawat Ophiolite Complex, Kurdistan Region, NE Iraq. Journal of Kirkuk University, 2,1-25.

Mohammad, Y.O., Cornell, D. H., Qaradaghi, J. H. and Mohammad, F. O., 2014. Geochemistry and Ar–Ar muscovite ages of the Daraban Leucogranite, Mawat Ophiolite, northeastern Iraq: implications for Arabia–Eurasia continental collision. Journal Asian Earth Science, 86, 151-165.

Mohammad Y. O.and Cornell D. H., 2017. U–Pb zircon geochronology of the Daraban leucogranite, Mawat ophiolite, Northeastern Iraq: a record of the subduction to collision history for the Arabia–Eurasia plates. Island Arc 26:e12188. https://doi.org/10.1111/iar.12188

Mohammad Y. O., 2020. Cumulate and tectonic dunite from Mawat ophiolite Kurdistan region northeastern Iraq: field evidence and mineral chemical constraints. Iraqi Bulltein Geological Mining, 16:15-33.

Moghadam, H. S.and Stern, R. J., 2015. Ophiolites of Iran: Keys to understanding the tectonic evolution of SW Asia: (II) Mesozoic ophiolites. Journal of Asian Earth Science, 100, 31-59.

Moghadam, H. S., Corfu, F., Stern, R. J.and Bakhsh, A. L., 2019. The Eastern Khoy metamorphic complex of NW Iran: a Jurassic ophiolite or continuation of the Sanandaj–Sirjan Zone? Journal Geological Society,176, 517-529.

Omrani, J., Agard, P., Whitechurch, H., Benoit, M., Prouteau, G.and Jolivet, L., 2008. Arc-magmatism and subduction history beneath the Zagros Mountains, Iran: a new report of adakites and geodynamic consequences. Lithos, 106, 380-398.

Pearce, J. A. and Norry, M. L., 1979. Petrogenetic implications of Ti, Zr, Y and Nb variations in volcanic rocks. Contrib. Mineral Petrology, 69, 33-47.

Pearce, J. A., 1983. Role of sub-continental lithosphere in magma genesis at active continental margins. In: Hawkesworth CJ, Nurry MJ (Eds) Continental Basalts and Mantle Xenoliths. Shiva Publishing, Nantwich, 230-249.

Pearce ,J. A., 2003. Supra-subduction zone ophiolites: The search for modern analogues. Geological Society America, 373, 269–294.

Pearce, J. A., 2014. Immobile element fingerprinting of ophiolites. Elements, 10,101–108.

Pearce, J. A., 1996. A user's guide to basalt discrimination diagrams. Trace element geochemistry of volcanic rocks: applications for massive sulphide exploration. Geological Association of Canada, 12, 79-113.

Pearce, J. A., 2008. Geochemical fingerprinting of oceanic basalts with applications to ophiolite classification and the search for Archean oceanic crust. Lithos, 100, 14–48.

Pearce, J. A. and Arculus, R. J., 2021. Boninites. Ensyclopedia of Geology, 2nd ed., 1,113-129.

Piccardo, G. B.and Guarnieri, L., 2011. Gabbro-norite cumulates from strongly depleted MORB melts in the Alpine–Apennine ophiolites. Lithos, 124, 200–214.

Pinto Linares, P. J., Levresse, G., Tritlla, J.and Gonzalez, M., 2008. Transitional adakite-like to calc-alkaline magmas in a continental extensional setting at La Paz Au-Cu skarn deposits, Mesa Central, Mexico: metallogenic implications. Revista Mexicana de Ciencias Geol Gicas, 25, 39–58.

Ross, P. S.and Bédard, J. H., 2009. Magmatic affinity of modern and ancient subalkaline volcanic rocks determined from trace-element discriminant diagrams. Canad. Journal Earth Science, 46, 823-839.

Reagan, M.K., Ishizuka, O., Stern, R.J., Kelley, K.A., Ohara, Y., Blichert-Toft, J., Bloomer, S.H., Cash, J., Fryer, P., Hanan, B.B., Hickey-Vargas, R., Ishii, T., Kimura, J.-I., Peate, D.W., Rowe, M.C., and Woods, M., 2010, Fore-arc basalts and subduction initiation in the Izu-Bonin-Mariana system: Geochemistry Geophysics Geosystems, 11, Q03X12,

Saccani, E., Padoa, E.and Photiades, A., 2003. Triassic mid-ocean ridge basalts from the Argolis Peninsula (Greece): new constraints for the early oceanization phases of the Neo-Tethyan Pindos basin. Geological Society London, 218, 1-19.

Saccani, E., Allahyari, K.and Rahimzadeh, B., 2014. Petrology and geochemistry of mafic magmatic rocks from the Sarve-Abad ophiolites (Kurdistan region, Iran): Evidence for interaction between MORB-type asthenosphere and OIB-type components in the southern Neo-Tethys Ocean. Tectonophysics, 621,132-147.

Saccani, E., Dilek, Y., Marroni, M.and Pandolfi, L., 2015. Continental margin ophiolites of Neotethys: remnants of ancient Ocean–Continent Transition Zone (OCTZ) Lithosphere and their geochemistry, mantle sources and melt evolution patterns. Episodes 38: 230-249.

Santosh, M., Teng, X. M., He X. F., Tang, L.and Yang, Q. Y., 2016. Discovery of Neoarchean suprasubduction zone ophiolite suite from Yishui Complex in the North China Craton. Gondwana Resources, 38,1-27.

Saunders, A. D., Norry, M. J.and Tarney, J., 1988. Origin of MORB and chemically-depleted mantle reservoirs: trace element constraints. Journal of Petroleum, 415-445.

Serri, G., 1981. The petrochemistry of ophiolite gabbroic complexes. A key for the classification of ophiolites into Low-Ti and High-Ti types. Earth Planet, 52, 203-212.

Shervais, J. W., 1982. Ti-V plots and the petrogenesis of modern and ophiolitic lavas. Earth planet, 59,101–118.

Shervais ,J. W., Reagan, M., Haugen, E., Almeev, R. R., Pearce, J.A., Prytulak, J., Ryan, J..G., Whattam, S. A., Godard, M., Chapman, T., Li H., Kurz, W., Nelson, W. R., Heaton, D., Kirchenbaur, M., Shimizu, K., Sakuyama, T., Li Y.and Vetter, S. K., 2019. Magmatic response to subduction initiation: Part 1. Fore-arc basalts of the Izu-Bonin arc from IODP Expedition 352. Geochem. Geophy, 20, 314-338.

Stern, R. J., Reagan, M., Ishizuka, O., Ohara, Y.and Whattam, S., 2012. To understand subduction initiation, study forearc crust: To understand forearc crust, study ophiolites. Lithosphere, 4, 469-483.

Stöcklin, J., 1968. Structural history and tectonics of Iran: a review. American Association Petroleum Geologists, 52, 1229–1258.

Sun, S. S., and McDonough, W.S., 1989. Chemical and isotopic systematics of oceanic basalts: implications for mantle composition and processes. Geological Society of London, 42, 313–345.

Veloso, E. A. E., Anma, R. and Yamazaki, T., 2005. Tectonic rotations during the Chile Ridge collision and obduction of the Taitao ophiolite (southern Chile). Island Arc, 14, 599-615.

Wehrmann, H., Hoernle, K., Garbe-Schönberg, D., Jacques, G., Mahlke, J.and Schumann, K., 2014. Insights from trace element geochemistry as to the roles of subduction zone geometry and subduction input on the chemistry of arc magmas. International Journal Earth Science, 103, 1929-1944.

Yumul, Jr. G.P., 2007. Westward younging disposition of Philippine ophiolites and its implication for arc evolution. Island Arc, 16, 306-317.

Zhang, Z., Xiao, W., Majidifard, M. R., Zhu, R., Wan, B., Ao, S., Chen, L., Rezaeian, M.and Esmaeili, R., 2017. Detrital zircon provenance analysis in the Zagros Orogen, SW Iran: implications for the amalgamation history of the Neo-Tethys. International Journal Earth Science,106, 1223-1238.